1-1-2017

Computational Study of the Effect of Interparticle Contact in Conductive Properties of Random Particulate Systems

Dongfang Zhao
University of Denver

Computational Study of the Effect of Interparticle Contact in Conductive Properties of

Random Particulate Systems

_____

A Thesis

Presented to

the Faculty of the Daniel Felix Ritchie School of Engineering and Computer Science

University of Denver

_____

In Partial Fulfillment

of the Requirements for the Degree

Master of Science

_____

by

Dongfang Zhao

March 2017

Advisor: Dr. Yun-Bo Yi

Author: Dongfang Zhao
Title: Computational Study of the Effect of Interparticle Contact in Conductive Properties of Random Particulate Systems
Advisor: Dr. Yun-Bo Yi
Degree Date: March 2017

Abstract

The effective conductivity of random particulate material system is computationally investigated using the Monte Carlo scheme and finite element method. A cubic system consisting of randomly-dispersed, equal-sized, deformable ellipsoids are modeled in this study. The steady-state conduction analysis along with a finite element analysis are performed to evaluate the electrical or thermal conductivity for the mechanical contact system. To represent more realistic material system, interfacial friction and gap conductance (or contact resistance) are included among the contacting particles. The Monte Carlo simulations are implemented to give a quantitative relationship between the effective conductivity and the inclusion volume fraction. Several parametric studies are performed to quantify the relationships, for example, (1) the particle number, (2) the particle shape, (3) the random distribution of particle, (4) the interfacial friction, (5) gap conductance. The study reveals the nonlinear relationship of the gap conductance with respect to the overall conductivity. Therefore, the mechanical properties of particulate system are strongly dependent on the interactions among inclusions. The study of microstructure of material is merited in advanced composite manufacture.

Acknowledgments

I want to thank to my research advisor Prof. Yi for providing me this unprecedented topic, in such a way that I have opportunities to step into the simulation world. I also would like to acknowledge the assistance of Prof. Yi, who support and encourage me to explore the scientific field. Thanks to all my lab mates who give me motivations and confidence to complete this work. In addition, thanks to the University of Denver administrators, Mechanical and Materials Engineering department faculties and staffs to let me get useful knowledge in my field. I enjoyed learning and living at the University of Denver.

Table of Contents

List of Figures

Chapter One: Introduction

1.1 Graphitic Lithium-ion battery

The Lithium-ion battery (Li-ion battery) is a kind of battery this is rechargeable while two electrodes with the constituent components of Li-ion battery are put into the electrolyte. The application of lithium metal along with the oxidant could always achieve the distinct chemistry performance, safety, or life length. For example, lithium cobalt oxide ($LiCoO_2$) can provide the high energy density while left the safety problems. Lithium iron phosphate ($LiFePO_4$), lithium nickel manganese cobalt oxide ($LiNiMnCoO_2$) can solve the safety issue with longer lives and inherent safety, but process the property of low energy density. The associated problems are due to the dendritic morphology of lithium metal, in which prevent the lithium metal behave as a composite matrix. The recent research has demonstrated the efficient solution is through the implementation of carbon-coated graphite as lithium intercalative host materials.

Increasing in electrical or thermal conductivity is obviously essential in graphic Li-ion battery. Earlier work have tried to add extra conductive particles in order to improve the conductivity for graphic Li-ion battery. But the most efficient and inexpensive way to achieve the desire conductivity is through compressing the Li-ion battery anodes into higher volume fraction. Fig. 1.1 shows the SEM images of Superior

Graphite (SL-20) anode under the pressure of 100 kg/cm^2, we can clearly detect the alteration of electrode's morphologies at the transverse direction under the application of compression pressure [53]. The compression model investigated in the current study is merited in optimization of graphic Li-ion battery.
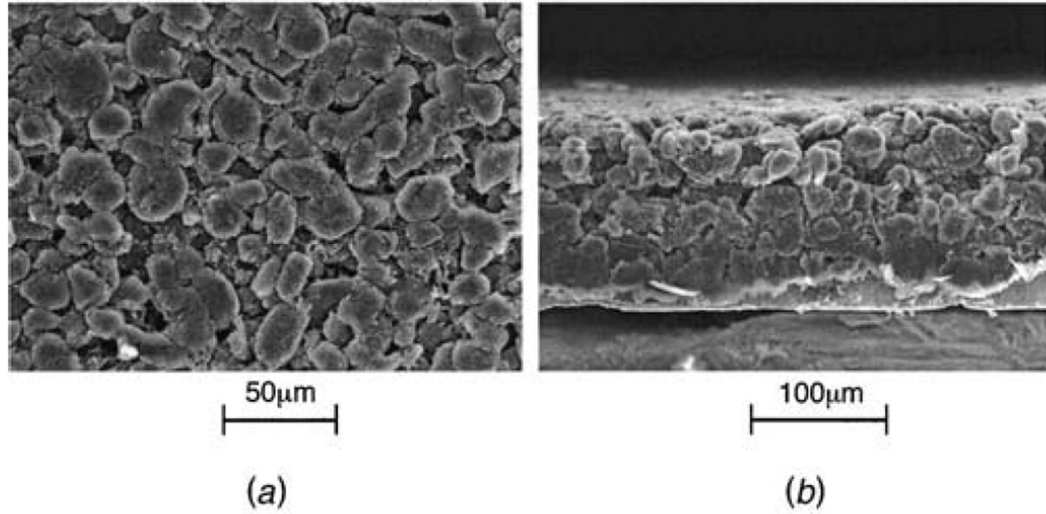
Fig 1. 1 SEM images of SL-20 anode materials under a pressure of 100 kg/m2. (a) a top view (b) a cross-sectional view

1.2 Introduction of Compression of Particulate System

Over the past few decades, the prediction of conductivity or percolation properties in designing heterogeneous particulate materials, which contain numerous shapes of particles, has been placed in an essential position in many scientific works. The main concerns are about to achieve the conductivity or percolation as large as possible. The previous works in this field have proven the fact that the increments in thermal or electrical conductivity can be obtained by compression of the particulate material into a higher volume fraction system. For example, Maleki et al. [1] along with the performed experiments demonstrated that the thermal conductivity values completely rely on the

compression pressure for negative electrode (NE) materials, which consist of synthetic graphite of various particles with varying polyvinylidene difluoride (PVDF) binder and carbon-black (C-Black) contents. Specifically, the relations showed that the thermal conductivity increased from 0.32 to 0.62 $W/m \cdot K$ at the temperature of 27°C when the compression pressure was increased from 250 to 575 kg/cm^2. Striebel et al. [2] found the fact that an increase in conductivity happened when implemented compression on the uncoated graphite. In addition, the compression of the amorphous-carbon-coated graphite anodes could strongly improve the reversible capacity (i.e., reduce the irreversibility loss,or ICL) and cycling efficiency. For example, the reversible capacity of GDR-6 graphite-additive anodes increased from 250 to 350 mAh/g with the value of 300kg/m^2 compression applied, while the reduction of ICL from 180 to 90 mAh/g for electrodes with no compression applied. The cyclability was improved for GDR-carbon anodes during compression without capacity lost, while the uncompressed one presented capacity inefficiency. Furthermore, the natural graphite anode cycling stability alsodepends on the compression pressure. The extent of SL20 anode could cycle up to 50 times in a lithium-metal half-cell compared to the uncompressed one. Gnanaraj et al. [3] studied the electroanalytical response of compressed or uncompressed LiCoO$_2$ electrodes, consisting of 15 wt% of graphite powder KS-6 as a conductive additive and 5 wt% of PVDF binder. The conclusion is that the performance of capacity and kinetics of compressed LiCoO$_2$ electrodes was much better than the performance of the uncompressed one. This is because the LiCoO$_2$ particles are hard enough to avoid the detriment of compression on the particle structure, so that the inter-particle contact and active mass won't be impeded while applying compression. Wang et al. [4] exhibited

coupled theoretical and experimental studies on Li-ion anodes with graphite additives to investigate the effectiveness of amorphous carbon coatings and anode compression on the improvements of anode electrical conductivity between the matrix and the current collector. Three distinct anode materials were investigated in their studies, which are SL-20 (a purified natural graphite produced by Superior Graphite), GDR-6 (6wt% amorphous carbon coating produced by Mitsui Mining), and GDR-14 (14wt% amorphous carbon coatings produced by Mitsui Mining). Each of them was tested under four levels of compression, which are 0, 100, 200, and 300 kg/cm^2. The experimental data showed that the addition of carbon coating is much more effective than the compression of anodes in improving the electrical conductivity of anode. More specifically, the increases in anode electrical conductivity for unpressed materials with addition of amorphous carbon coating can be presented as $\rho_{SL-20} > \rho_{GDR-6} > \rho_{GDR-14}$, although the experimental results also indicated the fact that the application of compression could obviously reduce the anode resistivity for SL-20 anodes. Fig. 1(a)-(d) shows the scanning electron microscope (SEM) images for SL-20 anodes with the application of 0, 100, 200 and 300 kg/cm^2. Fig. 2(a)-(d) shows the scanning electron microscope (SEM) images for GDR-6 anodes with the application of 0, 100, 200 and 300 kg/cm^2. Fig. 3(a)-(d) shows the scanning electron microscope (SEM) images for GDR-24 anodes with the application of 0, 100, 200 and 300 kg/cm^2. The semi-permeable particle can be clearly seen from the deformation in the transverse direction. The particle impermeability is essential in determining the percolation threshold of the compressed systems, which could strongly influence the conductivity of overall system.
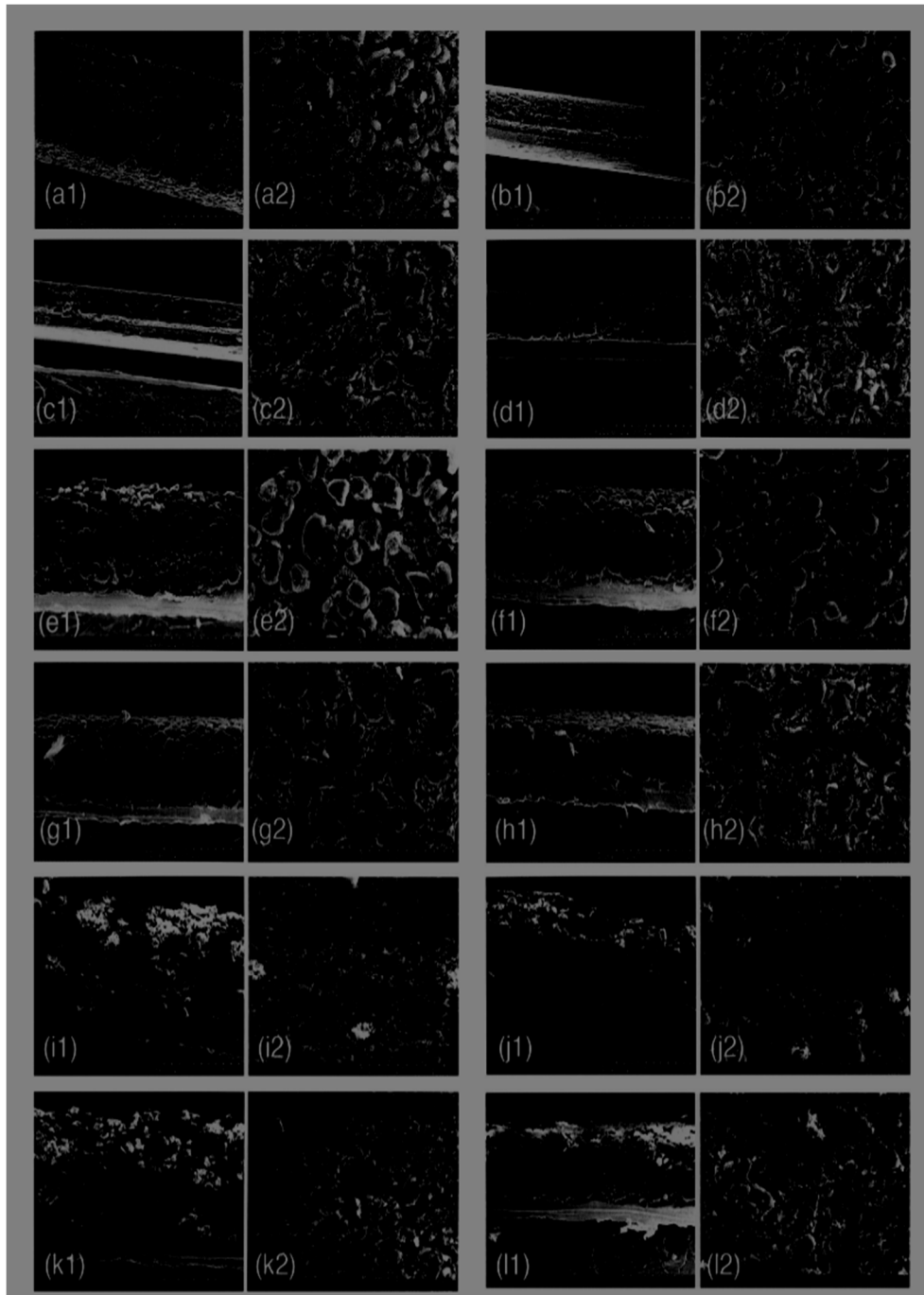
Fig 1. 2 SEM images of different kind of anodes after specific application of pressure

Maleki et al. [5] determined the thermal conductivity (k) values of negative electrode (NE) materials consisting of synthetic graphite with varying particle sizes,

various polyvinylidene difluoride (PVDF) binders, and carbon-black (C-Black) contents. The experiments of NE-material were conducted under the varied applications of compression levels. The experimental statistical data exhibited that the compression pressure is the primary role in affecting thermal conductivity of NE-material, and the graphite particle size, C-Black content and PVDF have less important effects. The results of their research showed that the maximum value of thermal conductivity can be accessible through the combination of the largest graphite particles (75 μm), the smallest C-Black content (5 wt.%) and the highest compression pressure (566 kg cm^{-2}). The author also studied the sole effect of compression pressure of thermal conductivity by setting all the other kinetic degrees of freedom as they were like in normal sample. The results showed the values of thermal conductivity of NE-material increases from 0.32 to 0.65 (W/m.k) as the compression pressure varying from 250 to 575 (kg cm^{-2}). The thermal conductivity of NE-material was shown to increase linearly with respect to the increases in compression pressure. However, too much compressive pressure will have harmful effects on battery performance due to the local stress concentration. For example, Gnanaraj et al. [3] pointed out an analysis, in which the performance (i.e., capacity and kinetics) would be damaged through the application of compression. They presented that the graphite electrodes, which contained 90 wt% graphite flakes (KS-6) and 10 wt% PVDF binder, exhibited a greater capacity and faster kinetics with in an uncompressed system. This is because the graphite electrodes have a morphology of soft, flat particles, which is easily destroyed under compression. The effects could thus block the contact between Li ions in solution species.

In our current study, we included the effects of realistic features on our compression models. For example, these features are represented by inter-particle frictions and contact resistance, which are not exhibited by idealized models.

1.3 Random close-packing and Maximum packing

Random packing of system inclusion (spheres, ellipsoids, spherocylinders, etc.) play an important role in the prediction of microstructure geometrical characteristics and then macrostructure properties. For example, the level of maximum densities achieved by packing rigid particles is considered as a fundamental way of investigating materials effective modulus or conductivity. Thus the algorithms applied in generating idealized randomly-arrange particulate system become the major concern. A large number of previous works have investigated the packing fraction η of the maximum densities possible from experimental packing operations or simulation packing method.

The definition of random close-packing (RCP) is proposed by Torquato et al. in their work [6]. They described RCP as a universal quantity that a collection of large, random-dispersed spherical system can achieve. This universal quantity is known as the maximum density of the material system. The packing fraction of equal-sized spherical inclusions can be distinctive with a different method of packing in experimental analysis. The existing literature [7] has obtained the value of RCP $\emptyset_c \approx 0.637$ through vertically vibrating the larger container with ball bearings in it for an adequate long time to achieve equilibrium. Another experimental analysis [8] made some improvements on the previous one resulting in achieving a denser packing. They poured the particles at a low rate into a horizontally vibrating containers. Computation simulation was also utilized to simulate

the possible maximum densities of random particulate system. For example, a prevailing algorithm including rate-dependent densification obtained $\emptyset_c$ lie between 0.642 and 0.649 [9]. A Monte Carlo method updated $\emptyset_c \approx 0.68$ [10]. And an algorithm called "drop and roll" produced $\emptyset_c$ a value of 0.60 [11]. The advantages of the first two algorithms over the last one are the system inclusions separately with each other.

However, the criteria of the above-mentioned cases are ill-defined since there is no analytical determination of the density of RCP. An updated value of packing fraction $\emptyset$ for equal-sized spheres is proved to be $\pi/\sqrt{18} \approx 0.7405$, using more recent rigor. This density is achieved in random close-packing face-centered cubic (FCC) lattice [6].

Maximum volume fraction (MVF) or maximum jamming fraction described by Torquato et al. in their work [6] is achievable of densities possible packing in a monodisperse material system with a particle of a given type. The position of a particle cannot be transferred as the adjustment of the position of all the rest particles. In this way, we called the system is jammed. For example, the maximum volume fraction for monodisperse spherical inclusions with face-centered cubic (FCC) structure has a value of 0.74 [12]. The jammed particulate system can be simulated through computer algorithm [13]. The aforementioned packing fraction is based on idealized models. However, incorporation with realistic, the real material systems might exhibit unpredictable features due to the imperfections. For example, the friction among particles might change the packing fraction slightly. The theoretical solution (i.e. percolation point) is identical to maximum jamming fraction only if infinite friction coefficients were assumed in the entire material system.

Primarily, the maximum packing fractions of the random particulate system are investigated via "growth algorithm" [14, 15]. Lubachevsky et al. proposed the packing system could exhibit various geometric features including polycrystalline textures with unpredictable grain boundaries and linear shear fractures [14]. W. S. Jodrey and E. M. Tory in their work [9] developed the random packing of the spherical system from a set of randomly distributed start points, each of which is representing the center of the inner and outer sphere. The inner spheres defined as the real particles were initially put in the system, while the outer sphere is a nominal one by expanding the inner diameter with a size factor. In their algorithms, the overlaps among sphere were minimized by moving the two overlapped spheres as equal distance along the center-to-center line in the opposite direction while reducing the diameter of outer spheres in each step. The moving among two overlapped particles may cause new overlaps with adjacent particles; center-to-center distance is calculated for each particle with adjacent touching ones, but if the overlap corresponding with its center-to-center line could be changed by the minimizing of the worst overlap, then this center-to-center line would not be considered. The criteria involved is increasing the center-to-center line up to the value of 1.3, corresponding to η=0.666. Fig. 1.2 (a)-(b) shows the criteria as mentioned above. The length of two diameters approaching each other after several interactions and the algorithms run until the diameter of outer spheres shrinking to the same value as the inner spheres.
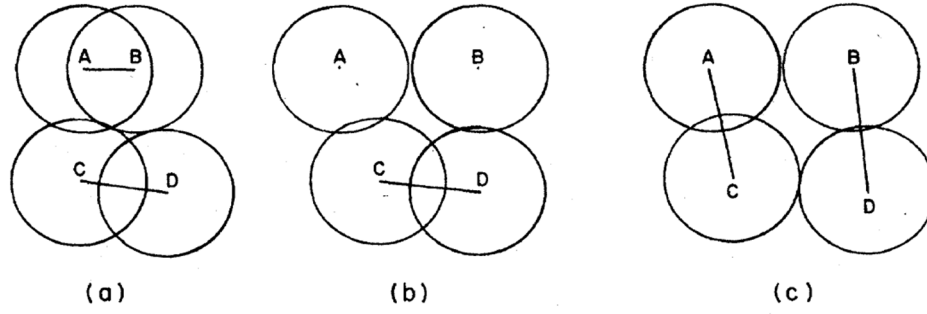
Fig 1. 3 Criteria in determination overlaps in a four-sphere-system. (a) The shortest center-to-center line AB and CD representing the worst overlaps in this step. Line AC and BD are not considered for not as worst as AB. (b) The worst overlap involving C and D

The simulation techniques are developed not only for creating random packings for spherical inclusions [16], but for spherocylinders [17] with the given aspect ratio $\alpha = 160.0$. Bezrukov et al. generated randomly-dispersed spheres using two algorithms in their work. The first one is the force-biased algorithm with production of high density packing, and the second one is the sedimentation algorithm which yields lower density of packing with weak anisotropy. In addition, the geometric characteristics (i.e. porosity, volume fraction, and pair correlation function) of the system were investigated. These parameters served as a bridge to connect and realize the comparisons between experimental results and simulation results. However, Williams et al developed a simulation technique for generating the maximum densities possible random-oriented system of spherocylinders. The upper limit of packing density they reach is $\emptyset = 0.70$ for very short spherocylinders, this result turned out to have a relation with respect to the aspect ratio.

1.4 Method for Predicting Effective Conductivity

Over the past few years, there is a growing interest in the heterogeneous particulate system and fiber enforced composites [18, 19]. Especially, the effective material properties (i.e. effective conductivity, or effective modulus, or percolation threshold) is becoming the major concerns in the heterogeneous material [20, 21]. The analytical or numerical methods can be solely or combine used to achieve maximum possible of material elastic modulus and effective conductivity [22, 23]. Numerous previous works have been done for prediction of percolation threshold, which is concerned as a fundamental step in determining material properties. For example, Yi and Sastry have developed an analytic solution on determining the percolative properties (i.e. statistical cluster properties) for two-dimensional (2D) and three-dimensional (3D) permeable ellipsoids [24]. The literature is not only working on predicting the percolation threshold of the particulate system, but also on the elastic modulus, and effective conductivity of fibrous networks [25, 26] and the particulate system as a representation [4] was also analyzed computationally. Yi studied the void percolation for the particulate system of identical ellipsoids of resolution using the discretization method [27]. The effective conductivity of the void phase of the system is investigated through finite element method. The results show these two material properties are strongly dependent on the geometrical shape of particles. In another word, neither the void percolation threshold nor the equivalent conductivity obtained from the particulate system of spherical inclusion can be directly applied to solving the problem including ellipsoidal particulate material, especially for the ellipsoids revolution with large aspect ratio. Some previous works

trying to predict the effective conductivity or effective modulus of the graphite particles in Li-ion electrodes were implemented a simplified model for the overlapping portion. More specifically, some parts of the two particles were assumed as a merged joint if their spatial locations were overlapped. Obviously, the contact resistance among particle interfaces is neglect in this simplified model. But none of the existing material is perfect; the mechanical impurity appeared among contact surfaces of particles due to the uncontrollable manufacturing process at some point. Especially, the contact resistance cannot be disregarded when the particles were covered by impermeable coating layers or got rough surfaces. The overall effective conductivity or effective modulus would be overestimated if the interparticle contact resistance were not considered. In our current analysis, we include the effect of contact resistance by involving "gap conductance," which means the finite value of contact resistance, it starts to have effect when the distance is below a specific pre-defined threshold for two approaching particles.

In stochastic fibrous networks, the simplified models with two-dimension (2D) [28, 29] or three-dimension (3D) [30] of constituent fibers were investigated in the prediction of percolation thresholds. Their works all show the geometric waviness of random fibrous networks definitely changed the mechanical properties, for example, the percolation threshold increased with "curl ratio". Although these models were somehow able to predict the tendency of the material properties, the assumed overlapping simplified structure has some limitations when the contact starts to play a role among carbon atoms on the tube walls. Thus, the interfacial computation must be included in contacting problem, despite some exceptions in some related work.

Previous works in this area have achieved significant accomplishments in predicting effective conductivity. A lot of mature theories were established, one of the most well-known approaches is called effective medium theories (EMTs), which can provide qualitative predictions of multiphase particulate materials with various volume fractions of particles [31]. Applications and Examples of EMTs include the Maxwell approximation [32], the self-consistent approximation [33], the linear rules of mixing [34], and the differential effective medium theory [35]. Tawerghi and Yi in their research showed the several schemes of predicting elastic modulus and effective conductivity in the application of effective medium theories [36]. Equation (1.3.1) K represents bulk modulus. Equation (1.3.2) G is the shear modulus. Equations (1.3.3)-(1.3.5) represent the Maxwell approach in describing the effective elastic modulus and conductivity of two-dimensional or three-dimensional spherical systems. Equation (1.3.6) was used to get the analytical solutions for circular void inclusions. Also this system was considered to have incompressible matrix leading to $\frac{K_2}{K_1} = \infty$, and the circular voids are cavities resulting in $K_2 = G_2 = 0$.

$$K = \frac{E}{[3(1 - 2\vartheta)]} \tag{1.1}$$

$$G = \frac{E}{[2(1 + \vartheta)]} \tag{1.2}$$

$$\frac{G_e - G_1}{G_e + H_1} = \emptyset_2 [\frac{G_2 - G_1}{G_2 + H_1}] \tag{1.3}$$

$$H_i = \frac{G_i[\frac{dK_i}{2} + \frac{(d+1)(d-2)G_i}{d}]}{K_i + 2G_i}, \qquad i = 1, 2, \tag{1.4}$$

$$\frac{\sigma_e - \sigma_1}{\sigma_e + (d-1)\sigma_1} = \emptyset_2 \left[\frac{\sigma_e - \sigma_1}{\sigma_2 + (d-1)\sigma_1}\right] \tag{1.5}$$

$$\frac{G_e}{G_1} = \frac{d(1-\emptyset_2)}{d-2\emptyset_2}, \qquad K_2 = G_2 = 0, \qquad \frac{K_1}{G_1} = \infty \tag{1.6}$$

In the above equations, E is the elastic modulus and ϑ is Poisson's ratio. The subscripts '1' and '2' corresponding to the matrix phase and the inclusion phase, respectively, $\emptyset_2$ is the volume fraction of the inclusion (summation of the volume fractions of the matrix and inclusions is equal to 1). G_e, G_1 and G_2 are the overall effective shear modulus, the shear modulus of the matrix, the shear modulus of the inclusions, respectively.

Another application of EMTs is the self-consistent (SC) approximation. The schemes of this approach are shown in Equations (1.3.7)-(1.3.11). Equation (1.3.12) is the self-consistent approximation for void inclusions, and the matrix is still based on the assumptions of incompressible as the above one.

$$\sum_{j=1}^{M} \emptyset_2 \frac{G_j - G_e}{G_j + H_e} = 0 \tag{1.7}$$

$$H_e = \frac{G_e[\frac{dK_e}{2} + (d+1)(d-1)G_e/d}{K_e + 2G_e} \tag{1.8}$$

$$\sum_{j=1}^{M} \emptyset_2 \frac{\sigma_j - \sigma_e}{\sigma_j + (d-1)\sigma_e} = 0 \tag{1.9}$$

$$\sigma_e = \frac{\alpha + \sqrt{\alpha^2 + 4(d-1)\sigma_1\sigma_2}}{2(d-1)} \tag{1.10}$$

$$\alpha = \sigma_1(d\emptyset_1 - 1) + \sigma_2(d\emptyset_2 - 1) \tag{1.11}$$

$$\frac{G_e}{G_1} = \frac{d[(d-1) - (d+1)\emptyset_2]}{d(d-1) - 2\emptyset_2} \tag{1.12}$$

Where M is the number of various types of inclusions.

Finally, the mostly indirect one is the effective differential medium (DEM) approximation. The equations described this approach are shown in Equation (1.3.13) and (1.3.14) as follow:

$$(1 - \emptyset_2)\frac{dG_e}{d\emptyset_2} = [G_j + H_e]\frac{G_2 - G_e}{G_2 + H_e} \tag{1.13}$$

$$(\frac{\sigma_2 - \sigma_e}{\sigma_2 - \sigma_1})(\frac{\sigma_1}{\sigma_e})^{1/d} = 1 - \emptyset_2 \tag{1.14}$$

A lot of work shown successfully implement of EMTs in predicting material properties of the random particulate system. For example, Mondescu and Muthukumar's research accomplished with EMTs deducted the analytical solutions for lower volume fraction, randomly-dispersed-particle system [37]

However, in some cases the accuracy associates with implement of EMTs is limited. It turned out to be unable to quantitatively predict the material properties in some situations involving random-dispersed particles. Garboczi and Berryman using two methods EMTs and finite element computations to investigate elastic modulus of a multiphase materials or composites [38]. They implied the implicit differential effective medium theory (D-EMT) and addressed the uncertainty of this approximation through the comparisons with actual known microstructures and phase modulus. These comparisons show only a small percentage of them are agreed with each other. Other evidence showed the inefficiency of EMTs is proved in research [39, 40]. The conclusions they reach is

that the effective conductivity and predicted percolation threshold based on EMTs did not show good agreement with experimental data for the particulate system at a lower volume fraction of particles.

In addition, there is still presented some work with applications of another approach for examining material properties. For example, one called homogenization methods were presented in Okada's work [41], they derived the formulations using boundary element method for heterogeneous elastic materials having periodic microstructure. Unfortunately, these analytical solutions would more or less fail in some situations. Thus, the computational approach has been employed to investigate the material properties. The powerful representative computational methods turned out to be Monte Carlo simulation techniques and Finite element analysis. In literature, Pike and Seager successfully investigated material conduction behavior and percolation threshold of regular or random models by implying two and three-dimensional Monte Carlo schemes [42]. The computational model was also implemented in studying the effect of hard-core interactions, probabilistic and deterministic bonding parameters, and varied functional form of the bonding criterion.

Studying the interparticle interactions effect on the material conductivity is of importance in this study. Many previous work turned out to be able to establish this connection. For example, Torquato and Rintoul constructed rigorous bounds on the effective conductivity for interfacial interactions among inclusions and enforced matrix [43]. The bounds were turned out to be accurate prediction thermal conductivity of the material system of metallic particles in epoxy matrices with respect to different values of the Kapitza resistance. Miloh and Benveniste derived dilute approximations to study the

16

conductivity of composite media with ellipsoidal inhomogeneity and highly conducting interfaces [44]. Wei and Poon [45], who investigated effective thermal conductivity of graded nonlinear composites with cylindrical inclusions embedded into a homogeneous matrix using the perturbation expansion method. The interestingly part of their work is they included thermal contact resistance on the inclusion interfaces, resulting in a nonlinear effective medium approximation of supposed composites. Benveniste [46] also developed a regular interface model for an arbitrarily curved three-dimensional interphase between two anisotropic particles.

1.5 Monte Carlo Schemes

Monte Carlo methods (or Monte Carlo experiments) are consisting a large number of computational algorithms. This computational approach would obtain numerically converged results through varying the repeated random sampling; typically the simulation needs to run several times to get an acknowledgment of the unknown probability distributions of the complex system. They have a broad range of influences, for example, they can be used in mathematical, physical, or even economy world. The simulation results extracted need to be analyzed to determine the characteristics of the object of interests. The procedures of how it work is listed [47]:

(1) Generation of a randomly-dispersed particulate system.

(2) Summarized and updated the new possible positions of these particles in a set and calculate the possibility of movement to each these sets.

(3) Select one of these sets randomly followed the computed probabilities.

(4) Select a location randomly within the chosen set

(5) Exert the operations of accepting or rejecting the resulting configuration based on the overlaps among particles.

Obviously, Monte Carlo simulation have some advantages over the other computational simulation algorithms. The advantages are listing as follow:

(1) The probability function can be directly and simply access by the model without any assumptions.

(2) The Monte Carlo algorithms are straightforward, we can understand their procedures with no need to gather a very high level of mathematics knowledge, just basic is enough.

(3) The changing of parameters can be directly reflected by the changing of system behavior. The accuracy of the simulation results dependent on the number of repeated runs.

1.6 Finite Element Analysis (FEA)

The finite element analysis (FEA), also called finite element method (FEM), is an efficient and influential numerical method used in various application field to derive the approximate solutions of the boundary-issued partial differential equations (PDE). In its algorithms, it divides a large physical body into tons of small, simple parts called finite elements with several nodes inside each of them. These nodes used as representing the configuration of elements and storing mechanics information. FEA then extend connection and combination of the PDE of each element into a larger PDE system that can represent the mechanical properties of the entire model. The global system equations

can be then solved through the specified numerical technique and the initial conditions of the original problem to attain the numerical solution.

Numerous earlier work has successfully implement FEA for approximate solutions to a variety of complex engineering problems. Nayak et al. [48] have implemented FEM to investigate the effective thermal conductivity of pine wood dust filled epoxy composites using finite-element commercial code ANSYS. The microstructure of the composites with various filler concentrations in the range of 6~36 vol.% was simulated through three-dimensional spheres-in-cube lattice array model. The study showed that the thermal conductivity of epoxy resin would be decreased by including pine wood dust and filler. The more percentage content of filler, the higher amplitude in thermal conductivity would drop. In detail, 6.5 vol.% of filler would result in the conductivity of epoxy resin decreased by 19.8%, and 36 vol.% of filler content would achieve a 57.3% reduction in the overall conductivity. Also, the validation of numerical calculation one (finite-element analysis) is confirmed by comparing it with the existing theoretical models and experimental data. The more complicated case, the composites consisting of a continuous matrix phase with dilute concentrations of dispersions of spherical, cylindrical or flat plate geometry with a thermal barrier resistance among the components interface, was analyzed through finite-element analysis [49]. The results demonstrated that both volume fraction of the dispersed phase and the dispersion size could affect the overall thermal conductivity with the existence of interfacial thermal barrier resistance. Also, the thermal conductivity of composites is independent of the dimensions of the microstructure with no interfacial thermal barrier resistance involved. Douglas et. al [50] combined finite

element method and finite difference method to deal with a parabolic problem of the form $cu_t + bu_x - (au_x)_x = f$ with error estimation on various problems.

The model typically has different geometry when performing the parametric study. Thus FEA requires for regeneration of a new model for each geometry, which would result in the intensive numerical procedure. However, the FEA commercial code such as Abaqus or ANASYS has the functionality called the generation of INP file including the geometric description and simulation parameter definition. This commercial software for finite-element analysis could help overcoming the difficulties in model generation. For example, Abaqus is a numerical solver for finite-element simulation with a various application in implicit or explicit analysis, steady-state heat transfer or thermodynamic situation, vibration problem, and acoustic and electromagnetic area. The main procedures in the finite-element analysis include generation of elements, parameter representation of mechanical properties, numerically solution calculation, and visualization of the results. The mesh generation process can be automatic and thus the target variable field can be determined without establishing analytical models. Shimada and Gossard [51] developed an algorithm as a new computational method to generate a fully-automatic triangular mesh of the trimmed parametric surfaces. The domain geometry and a node-spacing function work as input in this method and the mesh or a set of inter-connected triangles were generated based on the pre-defined requirements. The advantages of this kind method are that it can work as a computational and optimization tool of simulating variable fields (i.e. thermal conductivity) of materials with several contents without analytical models. In this study, we will imply Abaqus to perform the explicit finite element analysis on the deformable particles.

Until now, there is not too much work done in predicting electrical or thermal conductivity on the top of microstructure characteristics or particle interactions (i.e. interfacial friction or contact resistance among surfaces). Zhang and Yi [26] performed a study on the transport properties of three-dimensional fibrous networks, which is modeled as randomly-dispersed three-dimensional cylinders with a nonconductive body covered by a conductive coating layer. In their study, finite-element method was used to predict the effective thermal conductivity of the entire system and Monte Carlo simulation was performed to quantify the relations between the conductivity with the effecting factors such as the volume fraction of particles, the solidity of fibers, the thickness of the coating layer and so on. The solid body was discretized into a finite element mesh through the commercial code MATLAB® and COMSOL® and then conduct the generation of indices of points for three-dimensional Delaunay tessellation using the previous nodes. In their results, the effect of fiber orientation angle on conductivity cannot be neglected. The maximum value of overall conductivity is obtained while the fibers are aligned with the direction of electric current or the applied potential gradient.

Chapter Two: Simulation Method for Randomly-Dispersed Ellipsoidal System

In this study, we consider a system of randomly-dispersed, impermeable, and equisized ellipsoidal inclusions with negligible thickness distributed in a unit cell. The non-overlapped and randomly-arranged system of particles is generated with the incorporation of a series of dynamic collision algorithms. The contact behavior of deformed particles is simulated by compression of the system via finite element analysis. The effective conductivity of system particulate materials is evaluated by performing steady-state heat transfer analysis.

2.1 Generation of a System of Randomly-arranged Ellipsoids

2.1.1 Collision algorithms

In this study, the generated particles were assumed to be equally-sized tri-axial impermeable ellipsoids and the collisions were regarded as fully elastic that no energy was lost during the process. The randomly dispersed inclusions were developed inside a unit cell. The generation procedure of random particulate system not only required the center-point location dispersed randomly but also assumed the Euler angles of the axes to obey the prescribed density functions of probability. To avoid overlaps, we then deployed dynamic algorithms in which random parameters such as initial positions of the

center-points of each inclusion and random velocities that allow rigid body collision of particle-particle and particle-wall were assigned. In the previous works, the so-called "maximal packing fractions" in random particulate system were investigated by deployment of growth algorithms, in which the initial diameters of particles were assigned a "growth factor" resulting in a nominal outer sphere that involved in elastic collisions and is terminated when the further growth of the actual diameter of inclusions becomes impossible [9]. In this study, we neglect the successive growth rate of the actual diameter since our intents are not concentrated on arranging particles to achieve maximum packing fractions, but we keep the technique of expanding the actual diameters with a size factor and perform collision processing with the expanded outer particles in order to guarantee the actual particles are separated.

The initial randomly generated particles with random parameters were distributed in a unit cell. We employed the technique for the particle generation scheme that Yi, Wang and Sastry developed in their works: compression of packed particulate systems [53]. Firstly, the initial positions described as the center-point position $X_0=(x_0, y_0, z_0)$ of each ellipsoid were created as the equations as follows:

$$dd=1.1 \times max(a, b, c) \tag{2.1}$$

$$x_0=(cellx-dd) \times rand(0, 1) \tag{2.2}$$

$$y_0=(celly-dd) \times rand(0, 1) \tag{2.3}$$

$$z_0=(cellz-dd) \times rand(0, 1) \tag{2.4}$$

Where cellx=celly=cellz=1 that is the boundary of the cell in x, y, z directions, respectively. The Matlab function rand(0,1) creates random numbers between 0 and 1.

The parameters a, b, c are three semi-axis lengths of the ellipsoids. A parameter is set to ensure the randomly-generated ellipsoids would not exceed the boundary of the cell and the range of x, y, z is between $[\max(a,b,c) \quad (1\text{-}1.1 \times \max(a,b,c))]$. All the parameters distributed in this study are dimensionless. The initial orientation angles Θ (θ, μ, γ) were created between the range of 0 to π. The motion of each ellipsoid was defined by the linear velocity $V=(v_x, v_y, v_z)$ and rotational velocity $\dot{\Theta}=(\dot{\theta}, \dot{\mu}, \dot{\gamma})$ in the local coordinate system, or it can be presented as $\Omega=(\Omega_x, \Omega_y, \Omega_z)$ in the global coordinate system. The range of linear velocity is set randomly to between -1 and 1, and the rotational velocity varies from -3 to 3.

Developing efficient methods for inter-particle contact or overlap detection is of importance in our study. For spherical inclusions, the criterion in contact or overlap detection could be simply determined by comparisons between the radius *a* and the distance of the center-point of two spheres as follows, since these two parameters could definitely characterize the particle location and geometry.

$$\sqrt{(x_1 - x_2)^2 + (y_1 - y_2)^2 + (z_1 - z_2)^2} = \begin{cases} \leq 2a, & overlap. \\ > 2a, & seperate. \end{cases} \tag{2.5}$$

However, it is more intensive to derive the contact or overlap criterion for ellipsoidal inclusions, whose locations and geometry would be defined by not only the center-point location but also the orientation angles. The following equation can be used to express the added complexity of ellipsoids:

$$\frac{u^2}{a^2} + \frac{v^2}{b^2} + \frac{w^2}{c^2} = 1 \tag{2.6}$$

Where

$$\begin{bmatrix} u \\ v \\ w \end{bmatrix} = R \begin{bmatrix} x - x_0 \\ y - y_0 \\ z - z_0 \end{bmatrix} \tag{2.7}$$

In which (x_0, y_0, z_0) is the center-point coordinate of the ellipsoid, and R is the rotational matrix. In $\mathbb{R}^3$, rotations about x, y, z directions could be expressed as

$$R_x(\theta) = \begin{bmatrix} 1 & 0 & 0 \\ 0 & cos\theta & sin\theta \\ 0 & -sin\theta & cos\theta \end{bmatrix} \tag{2.8}$$

$$R_y(\mu) = \begin{bmatrix} cos\mu & 0 & -sin\mu \\ 0 & 1 & 0 \\ sin\mu & 0 & cos\mu \end{bmatrix} \tag{2.9}$$

$$R_z(\gamma) = \begin{bmatrix} cos\gamma & sin\gamma & 0 \\ -sin\gamma & cos\gamma & 0 \\ 0 & 0 & 1 \end{bmatrix} \tag{2.10}$$

The rotational matrix R can be calculated by composing three rotations about each of the corresponding axes, due to Euler's rotation theorem, as the following equation:

$$R = R_x(\theta)R_y(\mu)R_z(\gamma) = \begin{bmatrix} R_{11} & R_{12} & R_{13} \\ R_{21} & R_{22} & R_{23} \\ R_{31} & R_{32} & R_{33} \end{bmatrix}$$

$$= \begin{bmatrix} \cos\gamma\cos\mu\cos\theta - \sin\mu\sin\gamma & -\sin\gamma\cos\theta\cos\mu - \sin\mu\cos\gamma & \sin\theta\cos\mu \\ \cos\gamma\cos\theta\sin\mu + \cos\mu\sin\gamma & \cos\gamma\cos\mu - \cos\theta\sin\mu\sin\gamma & \sin\theta\sin\mu \\ -\cos\gamma\sin\theta & \sin\theta\sin\gamma & \cos\theta \end{bmatrix} \tag{2.11}$$

After the initial parameters had been generated, we began the deployment of rigid body algorithms that would help with avoiding overlaps between particles and arranging the particles into appropriate final positions. In the algorithms, each inclusion was given an initial velocity and allowed rigid body collisions with specific determination criteria implemented. This algorithm was run over thousands of iterations until there were no overlaps detected among the inclusions. The process usually ran 4000-5000 iterations, which the system is considered to be at steady-state, with a time step equal to 0.001. Also,

the particle number and particle size were predetermined to make sure the initial volume

fraction was constant. The repulsive forces coupling between the contacting parts of the

particles implement with rigid body collision algorithms were used to rectify the initial

overlaps over particle-particle and particle-wall. The following equation could present an

arbitrary point $X=(x, y, z)$ on the surface of an ellipsoid with its attributes:

$$(X - X_0)^T R^T B R (X - X_0) = 1 \qquad (2.12)$$

Where B is the characteristic matrix of ellipsoid

$$B = \begin{bmatrix} 1/c^2 & 0 & 0 \\ 0 & 1/b^2 & 0 \\ 0 & 0 & 1/a^2 \end{bmatrix} \qquad (2.13)$$

And R is the rotational matrix which is given above.

The chosen of extreme points on the surface of the ellipsoid are essential steps in

determining if the collision will occur between particles with their adjacent walls or

between particles. When we are detecting whether the ellipsoids will have a collision

possibility with the walls, the extreme points are defined as the surface points that have

the shortest distance with the adjacent walls in x, y, or z directions, for example the

extreme point in x direction will collide with the wall that is perpendicular to the x-axis if

the pre-determined conditions have been satisfied. In this study, we select three extreme

points which could reflect the collision possibility of each ellipsoid with six walls. The

definition of extreme points can be described as the following graph Fig. 2.1, in which x_0

is the coordinate of the center-point of the ellipsoid and x is the x- coordinate of the

surface point on the ellipsoid following the equation $\Delta x = x - x_0$. If either

pre-determined collision condition (1) $x < \Delta x$ or (2) $x > cellx - \Delta x$ is satisfied, the

specified ellipsoid will collide with the wall. The predetermined collision conditions of the extreme points in y and z are the like. During each iteration, we firstly resolve the possibility of collision within each ellipsoid and their adjacent wall by using three extreme points following the pre-determined criteria. Then we update the linear and rotational velocities of collision points. The next step is detecting the collision possibility of one ellipsoid with the rest and update its linear velocity, rotational velocity, x, y, z coordinates, and rotational matrix after collision. Each iteration ends when the analysis of collision has been done among each particle. The linear and rotational velocities of each ellipsoid will be updated whenever the collision happens, but the x, y, z coordinates of each ellipsoid were renewed only one time during each iteration. The initial overlapping particles system that finally becomes an overlap-free, randomly-dispersed particulate system is realized through the Monte Carlo collision detection algorithms during each iteration.
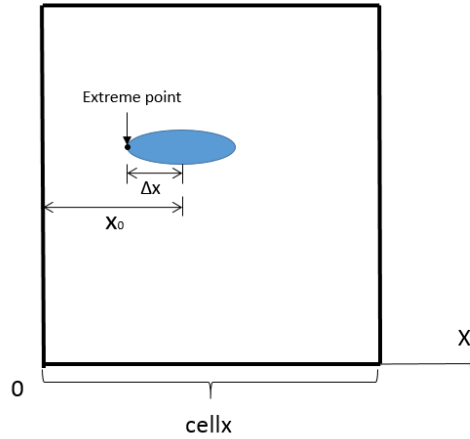

Fig 2. 1Extreme point selection

To calculate the extreme values (maximum and minimum values) of the ellipsoid in the z direction, for example, we set

$$\frac{\partial z}{\partial x} = 0, \qquad \frac{\partial z}{\partial y} = 0 \tag{2.14}$$

and, obtain the expressions of u, v, and w after simplification

$$u = \pm \sqrt{\frac{a^4 (R_{21} R_{32} - R_{22} R_{31})^2}{a^2 (R_{21} R_{32} - R_{22} R_{31})^2 + b^2 (R_{11} R_{32} - R_{12} R_{31})^2 + c^2 (R_{22} R_{11} - R_{12} R_{21})^2}} \tag{2.15}$$

$$v = -\frac{b^2}{a^2} \frac{R_{11} R_{32} - R_{12} R_{31}}{R_{21} R_{32} - R_{22} R_{31}} u \tag{2.16}$$

$$w = \frac{c^2}{a^2} \frac{R_{22} R_{11} - R_{12} R_{21}}{R_{21} R_{32} - R_{22} R_{31}} u \tag{2.17}$$

where R_{ij} is the components of the rotational matrix. Then we simplified the expression of u, v, and w using the rotational matrix R and get the extreme values of the surface points in z direction as follows:

$$\begin{bmatrix} x \\ y \\ z \end{bmatrix} = \begin{bmatrix} x_0 \\ y_0 \\ z_0 \end{bmatrix} \pm \frac{1}{\sqrt{a^2 \sin^2 \theta \cos^2 \mu + b^2 \sin^2 \theta \sin^2 \mu + c^2 \cos^2 \theta}}$$

$$\times \begin{bmatrix} \sin \theta \cos \theta \cos \gamma \, (a^2 \cos^2 \mu + b^2 \sin^2 \mu - c^2) + \sin \theta \sin \mu \cos \mu \sin \gamma (b^2 - a^2) \\ \sin \theta \sin \mu \cos \mu \cos \gamma \, (b^2 - a^2) - \sin \theta \cos \theta \sin \gamma \, (b^2 + a^2 - c^2) \\ a^2 \sin^2 \theta \cos^2 \mu + b^2 \sin^2 \theta \sin^2 \mu + c^2 \cos^2 \theta \end{bmatrix} \tag{2.18}$$

The extreme values in x and y directions can be derived in a similar way as we did in z direction. In summary, the extreme points $X=(x, y, z)$ on the surface of ellipsoids can be deducted as

$$C = \sqrt{a^2 R_{1k}{}^2 + b^2 R_{2k}{}^2 + c^2 R_{3k}{}^2} \tag{2.19}$$

$$\Delta x = x - x_0 = \pm \frac{a^2 R_{1k} R_{11} + b^2 R_{2k} R_{21} + c^2 R_{3k} R_{31}}{C} \tag{2.20}$$

$$\Delta y = y - y_0 = \pm \frac{a^2 R_{1k} R_{12} + b^2 R_{2k} R_{22} + c^2 R_{3k} R_{32}}{C} \tag{2.21}$$

$$\Delta z = z - z_0 = \pm \frac{a^2 R_{1k} R_{13} + b^2 R_{2k} R_{23} + c^2 R_{3k} R_{33}}{C} \tag{2.22}$$

Where k=1, 2, 3 in the x, y, z directions, respectively.

The linear and rotational velocities were recalculated after each collision at the time step. We implement the Equations (2.20) (2.21) (2.22) for updating the positions of extreme points on the surface of the ellipsoids during each iteration. And also we use the collision equation to renew the linear and rotational velocities of each ellipsoid. The following steps show the derivation of collision equations. The variations of linear and rotational velocities during collision range from V to $V + \Delta V$ and Ω to $\Omega + \Delta \Omega$, respectively. Their relation can be solved by conservation of energy in the resulting system as follows.

$$\Delta \Omega^T I \Omega + \Omega^T I \Delta \Omega + \Delta \Omega^T I \Delta \Omega + \Delta V^T M V + \Delta V^T M V + V^T M \Delta V + \Delta V^T M \Delta V = 0$$

Where I is the moment of inertia of particle, and M is the mass matrix of a particle.

$$M = \frac{4}{3} \pi abc\rho \begin{bmatrix} 1 & 0 & 0 \\ 0 & 1 & 0 \\ 0 & 0 & 1 \end{bmatrix} \tag{2.23}$$

And ρ is the density of the ellipsoids. Then letting r represent $X - X_0$, and n represent the normal direction of the surface at X, the balances of linear and angular momentum for an ellipsoid result in the following equation

$$\vec{r} \times \vec{P} = I \Delta \vec{\Omega} \tag{2.24}$$

And

$$\vec{P} = M\Delta\vec{V} \tag{2.25}$$

Where P is the linear momentum caused by the collision force between the rigid surface of the wall and the ellipsoid. We can rephrase the above relations by using $T = \vec{r} \times \vec{n} = (r_2 n_3 - r_3 n_2)\vec{i} + (r_3 n_1 - r_1 n_3)\vec{j} + (r_1 n_2 - r_2 n_1)\vec{k}$ and N as the matrix form of the normal, the equations could become

$$\Delta\Omega = I^{-1}TP \tag{2.26}$$

$$\Delta V = M^{-1}NP \tag{2.27}$$

Substitution Eq. (2.26) into Eq. (2.23) produces

$$\Delta\Omega = \frac{-2(N^T V + T^T \Omega)I^{-1}T}{|M^{-1}| + T^T I^{-1}T} \tag{2.28}$$

Considering energy and momentum, the collision equation between two ellipsoids can be inferred that

$$\Delta\Omega_i = \frac{-2(N^T(V_1 - V_2)) + (T_1{}^T \Omega_1 - T_2{}^T \Omega_2)}{|M_1{}^{-1}| + |M_2{}^{-1}| + (T_1{}^T I_1{}^{-1}T_1 + T_2{}^T I_2{}^{-1}T_2)} I_i{}^{-1}T_i \tag{2.29}$$

Where i=1, 2 are two specific particles involved in a collision.

The solutions for all positions of ellipsoids can be derived through the iteration in the simulation time

$$R_j\left(\Theta_j(t + \Delta t)\right) = R_j(\Omega_j \Delta t)R_j\left(\Theta_j(t)\right), \tag{2.30}$$

$$X_j(t + \Delta t) = X_j(t) + V_j \Delta t \tag{2.31}$$

Where j=1, 2,..., n; n is the total simulated number of inclusions in the system.

2.1.2 Visualization of the generated particulate system

The basic step of generating a unit sphere centered at the origin in Matlab$^{©}$ is using the embedded function "sphere(n)" which would create three (n+1)-by-(n+1) matrix arrays describing the coordinates of x, y, and z directions of the surface points. Then we use the parameters such as center-point positions, semi-axis lengths, and a rotational matrix of the ellipsoids to convert the unit sphere to the ellipsoid we investigated. In this study, we generate a sphere consisting of 60-by-60 faces (n=60) for the reason of generating relatively smooth and continuous surfaces of the sphere at the shortest computation time. The generated coordinates in the z-direction are the same in each row in the matrix, which means the coordinates of the surface points on a cutting face that is perpendicular to the z-axis could be presented by the numbers in the corresponding rows in x and y arrays. So we take each corresponding row (from the first row) in x, y and z arrays and assemble a new matrix r that represent the surface points of the sphere on a specific cutting face at z-direction. Then we have each row of matrix r multiplied by the semi-axis lengths a, b, c of the ellipsoids to achieve the size of ellipsoid we want, since the sphere is unit-size and centered at the origin. The new coordinates of the ellipsoids can be obtained by the rotational matrix multiplied by matrix r as presented in Eq. (2.33), since in two dimensions the rotation column vectors are achieved by means of its rotational matrix as followed
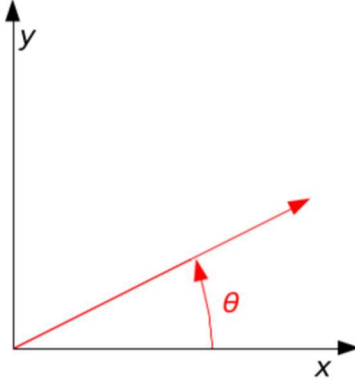
Fig 2. 2 Coordinate transformation

$$R(\theta) = \begin{bmatrix} cos\theta & -sin\theta \\ sin\theta & cos\theta \end{bmatrix} \tag{2.32}$$

$$\begin{bmatrix} x' \\ y' \end{bmatrix} = \begin{bmatrix} cos\theta & -sin\theta \\ sin\theta & cos\theta \end{bmatrix} \begin{bmatrix} x \\ y \end{bmatrix} \tag{2.33}$$

For rotation column vectors on the surface of ellipsoids

$$\begin{bmatrix} x' \\ y' \\ z' \end{bmatrix} = \begin{bmatrix} \cos\gamma\cos\mu\cos\theta - \sin\mu\sin\gamma & -\sin\gamma\cos\theta\cos\mu - \sin\mu\cos\gamma & \sin\theta\cos\mu \\ \cos\gamma\cos\theta\sin\mu + \cos\mu\sin\gamma & \cos\gamma\cos\mu - \cos\theta\sin\mu\sin\gamma & \sin\theta\sin\mu \\ -\cos\gamma\sin\theta & \sin\theta\sin\gamma & \cos\theta \end{bmatrix} \begin{bmatrix} x \\ y \\ z \end{bmatrix} \tag{2.34}$$

We define a 3×61 matrix r_0 whose first row is filled with the center-point coordinate in x-direction, the second row is the center-point coordinate in y-direction, and the third row is the center-point coordinate in z-direction. The updated matrix r is then added by the matrix r_0 to assign the ellipsoid to the right position. Then each row of matrix r is distributed to the corresponding row in xx, yy, and zz matrices that describe the location of each ellipsoid. This procedure is to calculate and update the coordinates of surface points of the sphere on all cutting-faces.

The Fig. 2.3 (a) (b) (c) show the regular ellipsoidal inclusions (prolate spheroid), the spherical particles and oblate spheroid.
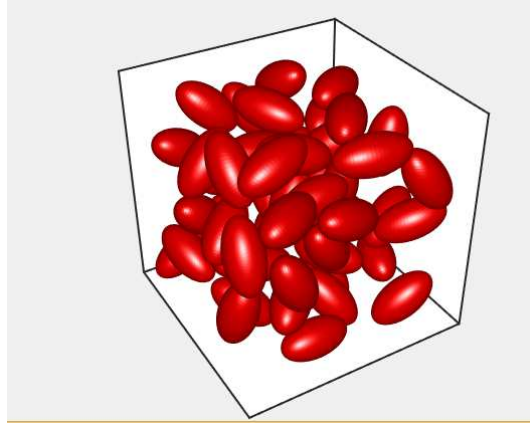
(a)
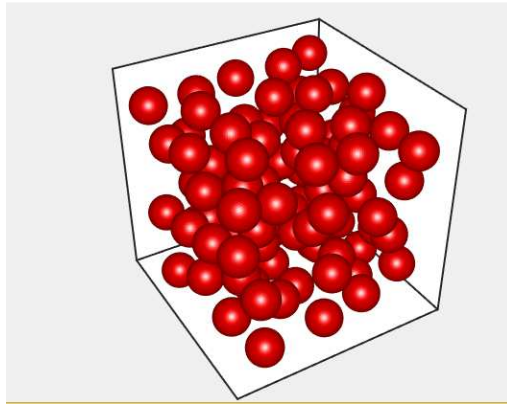
(b)

(c)

Fig 2. 3 Computer-generated models of (a) non-overlapping prolate spheroid (b) non-overlapping of spheres (c) non-overlapping oblate spheroid.

2.2 Simulation of Contact Behavior

2.2.1 Element selection and generation

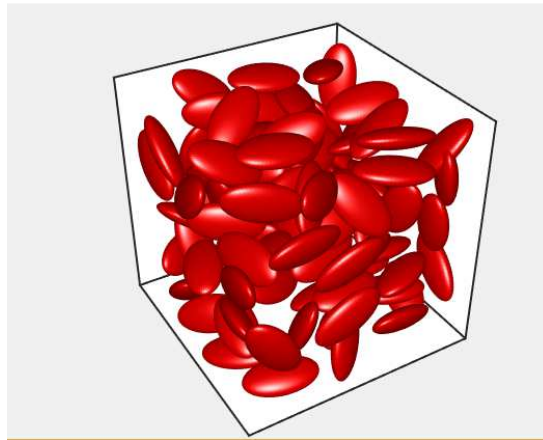In the second step, finite element meshing was performed on each generated ellipsoid from the first step. We assume the system inclusions as shell particles in such a way that the conductive contents lie exclusively on the surfaces of particles. Zhang and Yi [26] modeled the cylindrical fiber composites as a nonconductive core coated by a conductive layer and quantified the relation of system conductivity and percolation with coating layer thickness. They concluded that a higher effective conductivity can be obtained by the coated structure against the solid one as the same amount of conductive material applied, since the conductive material with a larger mean diameter of the coated one could thus have a higher possibility of contacting with others compared to the solid one, in which the conductive material concentrated within a small space.

The consideration of shell particles is due to the following reasons: (1) to reflect the reality, the operations that enable most nonconductive materials to obtain the property of conductivity are rendering them with conductive coating layer, (2) the finite element method investigated in this study requires finding approximate solutions for partial differential equations of each element with boundary values specified. The more elements generated in an analysis would lead to a greater number of partial differential equations to be solved and further resulting in a longer computing time. The shell particles have a fewer number of elements that generated only on the surface compared to elements of the same size in the solid body, in which longer simulating time is needed.

The mesh generation of the particles is a fundamental step in finite element analysis. In this study, we create a shell mesh with triangular elements on the surface of each inclusion using built-in automatic mesh generation algorithms inside the commercial code COMSOL$^©$ [54]. Fig. 2.4 shows the sphere that has been subdivided into finite triangular parts fulfilled by COMSOL$^©$ mesh generation algorithms. To avoid the possibility of inhomogeneous mesh density, which is curvature dependent, the parameters such as the curvature cutoff threshold and maximum element size are incorporated to prevent the occurrence of numerical inaccuracy that was caused by the local singularities. The tetrahedron finite element meshing was first generated on a single sphere and then replicated on the others by implemented geometric data of each specified ellipsoid. The methods of updating coordinates for ellipsoids were mentioned in the Visualization Section.Briefly speaking, the coordinates of each node of the sphere were multiplied by the ellipsoids semi-length a, b, c in corresponding x, y, and z directions. Then coordinates matrix times the rotational matrix of the ellipsoid were updated and finally the coordinate of each node in x, y, z directions was added to the center-point coordinates of ellipsoid x_0, y_0, z_0, respectively. The overall size of nodes is between 30,900 and 61,800. As for element type selection, it is definitely common that a lot of modeling issues must be considered when using different types of shell elements, for example, the S4 or S4R (4-node, quadrilateral, stress/displacement shell element (or with reduced integration)) is recommended in pure bending situations or to get solutions to problems involving high strains gradients. In the second step contact behavior analysis, we choose "S3R" (3-node triangular, general-purpose, conventional stress/displacement shell element with reduced integration, finite membrane strains) as element type of ellipsoidal particles, since the

S3R type of element we used here can provide accurate results in most loading situations. The reduced integration in the shell elements can form element stiffness while integrating mass matrix and distributing loadings exactly. In our three-dimension analysis, using reduced integrations could not only provide relatively more accurate results but also reduce simulating times. We believe that in "hard contact" situations that our particles cannot penetrate each other, it is much better to choose the first-order triangle or constant strain triangle we used here. Another important reason for choosing the first-order, reduced-integration elements is the best choice suitable for our solver ABAQUS/EXPLICIT® used in the contact analysis. In our third step conduction analysis, we choose the element type "DS3" (3-node triangular, heat transfer shell element), which is available only in ABAQUS/STANDARD®. The overall size of elements is between 61,600 and 123,200.
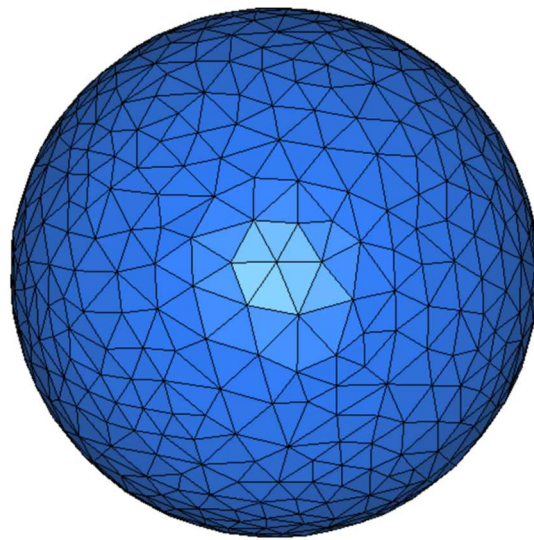

Fig 2. 4 Single meshed sphere

2.2.2 Simulation parameters selection

The finite element model parameters and material properties that used to construct ellipsoids in simulation process are listed in Table 2.1 and Table 2.2. These are selected and combined for the purpose of achieving the numerical converging results with the fast speed based on the pre-determined solution tolerance. The solution analyzing procedure is simulating in a long time scale, although it will result in a requirement of a large number of small time increments in the explicit analysis, in order to reduce the effect of inertia effects caused by the plate compression. The selection of simulation time lengths plays an essential role in our study. More specifically, the elastic deformation of the top set of particles in the system would become so significant so that they cannot transfer the loads to the bottom set as soon as possible if the domain walls move fairly fast. The results also wouldn't be acceptable if the domain walls move in an absolutely slow way, which results in the absence of local stresses developing when the stress waves go over the entire system. The value of simulation time 0.4 based on the plate displacement value 0.2 is chosen through a series of testing in our parameter study, which ensures our simulation results are independent of the compressing speed of domain walls.

2.2.3 Deformable contact model simulation

The two basic solving procedures implicit in ABAQUS/STANDARD$^{®}$ and explicit in ABAQUS/EXPLICIT$^{®}$ are most commonly used in solving nonlinear problems. Although certain static or quasi-static problems that can be simulated well with either program, ABAQUS/STANDARD$^{®}$ may have difficulty converging in solving problems

containing contact or material complexities, which would result in a large number of iterations. A large set of linear equations need to be solved in each iteration, and the iterations are repeated in each increment until the results are converged, which means the force equilibrium, moment equilibrium, and contact conditions are achieved at each node. Whereas ABAQUS/EXPLICIT$^{®}$ obtains the solution without iterating by explicitly advancing the kinematic state from the previous increment, even though a large number of time increments might be investigated in a certain analysis. Also, the time increment size is independent of the number of contact points and the complexity of the contact conditions in the explicit procedure. The three-dimensional models with complex contact interactions among several independent bodies always have a huge number of contacting points and the changing contact conditions simulated in our analysis would result in extremely small time increments or convergence difficulties. Thus, we, in this step, simulated the contact behavior between the deformable ellipsoidal particles via explicit finite element analysis in ABAQUS/EXPLICIT$^{®}$. Also, the quantities that used to calculate displacement and velocities at each node are already known when starting the increment in an explicit dynamic analysis so that the global mass and stiffness matrices are not required to form, which made the increment less intensive compared with that in the implicit procedure.

The same elastic material properties, Poisson's ratio 0.495 and Young's Modulus 1×10^{1}, was set to all the elements. Young's Modulus was setting a relatively small value to ensure the particles to be soft and deformable during compression. Poisson's ratio was set to avoid the changing among area during particle compression. The parameters used in explicit finite element analysis during particle compression are listed in Table 2.1. The

system of finite element meshing particles was discretized inside a constrained, unit cubical domain. The volume fraction of particles was obtained by the sum of total particle volumes divided by the volume of system cell corresponding at the specific position of the domain wall. The tri-axial particle semi-lengths in three directions x, y, and z were predestined through the criterion that the initial volume fraction would need to exceed the jamming fraction of rigid particles. During computational simulation, each of the six domain walls was compressed along either the x, y, or z direction; the two horizontal faces, the top, and the bottom faces, can only move vertically and the four vertical side faces can only move in the horizontal direction, while all of the rest of the degrees of freedom were fixed. The system domain was compressed by the six domain walls at a constant speed, leading the system of the domain as a cubical cell during the compression simulation. The surface interaction, i.e. inter-particle friction coefficient, and particle-container friction coefficient, was assigned to contact pairs, which is defined between the contacting particles as well as contacting of particles with cubical domain walls. The "all element based" option was investigated between these contact pairs for an all-inclusive element-based surface. Firstly, we investigate the contact pairs with frictionless contacting interactions in order to reduce the number of variables and simulation complexity, and in the following parametrical study we implement the friction interactions as well keeping some of the variables constant. The penalty friction formula, which was using friction coefficient in describing contact interaction properties, was investigated here to study the tangential behavior of contacting surfaces. The computational equations can be summarized as follows:

$$\tau_{crit} = \mu \times p$$

Where τ_{crit} is critical frictional shear stress at surface nodes, μ is the frictional coefficient, p is contact pressure at surface nodes (CPRESS).

Another issue is the inhomogeneity of the system during the particle compression procedure, in which the local density of the particles near the boundary faces are not equal to the particles inside the domain. This is due to the reason that the outside particles have the possibility to gather up and the density of interior remains unchanged when compressing the particles that are initially stable. The solutions for this issue are given each particle random velocities and allow them to move randomly while compressing the system. The step analysis was achieved by the generation of ABAQUS® input file, which contained the mesh information of particles, the material properties assigned, the surface contacting interactions between particle-particle or particle-wall, the defined appropriate boundary conditions, and the prescribed solver information.

Simulation time	Plate displacement	Inter-particle friction coefficient	Particle-container friction coefficient	Elastic modulus	Poisson's ratio	density	Shell thickness/radius a
0.4	0.2	0-1	0-1	10	0.495	1e-05	0.15

Table 2. 1 Parameters for contact behavior analysis during particle compression

2.3 Steady-state Conduction Analysis

In thermodynamics, we considered the steady-state conduction, which was constant, was enforced by the temperature gradient, which means the temperature fields in the energetic particles of the substance do not change after the system reaches an equilibrium state. Thus in a mathematic view, the partial derivatives of the system temperature with respect to time may either be zero or a non-zero constant. Also, the amount of heat flowing into and out the substance of particles is equivalent to the steady-state analysis.

According to the law of heat conduction (Fourier's law), it is known that the heat transfer rate through a layer is proportional to the negative temperature difference across the layer and to the surface area. This law can be presented in a differential form, through which we can look into the local heat flux density $\vec{q}$ is equivalent to thermal conductivity κ multiplied by the negative local temperature difference $-\Delta T$. The relations can be expressed as follows:

$$\vec{q} = -\kappa \Delta T \tag{2.35}$$

Where $\vec{q}$ is the time rate of heat flux, $W \cdot m^{-2}$. κ is the thermal conductivity of material, $W \cdot m^{-1} \cdot K^{-1}$. ΔT is the temperature difference through the surface layer, $K \cdot m^{-1}$.

Through the integral form as follows, we can look into the amount of energy flowing through the material body:

$$\frac{\partial Q}{\partial t} = -k \oiint_s \nabla T \cdot dS \tag{2.36}$$

Where $\frac{\partial Q}{\partial t}$ is the amount of heat transferred per unit time, and dS is an oriented surface area element.

In this step, an implicit finite element solving procedure in ABAQUS/STANDARD® is implemented to perform the steady-state conduction analysis, since the contact resistance (or "gap conductance") and transient analysis simulated here would result in a more expensive way of finding solutions and a requirement for extremely small time step when using an explicit finite element solving procedure.

In the third step, the simulation results, the displacement of each node, were exported to an ABAQUS® rpt file at the requested time interval (we use 30 intervals here),

each of which is related to a specific value of the varying volume fractions of inclusions, or a distinct situation of the compressing cubical domain walls. The displacement results were then used to update the nodal positions of the deformed tetrahedron finite element mesh at each interval, with which we can build the model for subsequent thermal conduction analysis. In addition, a steady-state heat transfer analysis was operated to investigate the effective conductivity of the updated ellipsoidal model. More specifically, the appropriate boundary conditions were established in such a way that a unit temperature was set on the top surface of the model whereas a zero temperature was set on the bottom of the model. The reactive heat flux happened under the temperature difference and the steady-state heat transfer conduction was computed by solving Laplace's equation. The temperature was the single left degree of freedom whereas other kinetic degrees of freedom were dismissed. The pre-determined conditions implemented to classify the node for the top set or for the bottom set, which is used to assign temperature gradient, are achieved by the comparisons between z-direction coordinates of each node. If the value for z-direction coordinate of the node is bigger than 0.079 (which is equal to 1-plate_displacement-0.01), the certified nodes belong to the top set. Or if the value for z-direction coordinate if the node is smaller than 0.21 (which is equal to plate_displacement+0.01), the certified nodes belong to the bottom set. The frequently used parameters in this conduction analysis in Table 2.2 are listed as follows. We set the parameter thermal expansion to be zero in order to prevent the material from expansion under the flowing of heat flux. It can be demonstrated that the summing of the nodal reactive flux is equal to the effective conductivity of the whole particulate system. The

effective conductivity calculated through this analysis can be applied in either electrical analysis or thermal analysis considering the results normalized.

The reciprocal of conductance is resistance, R, given by Eq. (2.37)

$$R = \frac{1}{\kappa} = \frac{(-\Delta T)}{\vec{q}}$$

(2.37)

The thermal contact resistance would drive the temperature to drop appreciably across the contacting interface since it is proportional to the negative temperature gradient across the material layer. The contact resistance was studied in this step through the written keywords "gap conductance" in ABAQUS$^{®}$ input file. It would definitely lower the effective conductivity as determined by either the contact pressure or the normal distance between two approaching surfaces. A scheme to lower the computational cost is investigated here, in which a constant gap conductance was supposed when the normal distance between two approaching surfaces reaches the threshold as 0.001.

Elastic Modulus	Density	conductivity	Specific heat	Thermal expansion	Gap conductance	Gap distance
1×10^{1}	1×10^{-05}	1×10^{0}	1×10^{-04}	0	1×10^{6}	0.001

Table 2. 2 Parameters for conduction analysis

For the conduction analysis of the system of identical ellipsoids, we investigated the efficient algorithms for detecting contact pairs that Yi and Sastry have used in their works [24]. The details of algorithms can be described as the following equations. We indicated u_1, u_2 as the unit vectors of the axes of revolution for two identical ellipsoids E_1 and E_2. The parameters *a* and *b* are the major and minor half-axes, *u* is the vector joining the center points of two ellipsoids. The essential and appreciable condition for two particles to be totally separated or to be tangential to each other is that the three following

equations (ψ,s_1,s_2) to be positive or zero, and as well as at least one of the quantities t_1, t_2 and h to be negative.

$$\xi = \frac{a}{b} - \frac{b}{a} \tag{2.38}$$

$$t_1 = 4 + \xi^2 (u_1 \times u_2)^2 - \frac{|u|}{b^2} + (\frac{1}{b^2} - \frac{1}{a^2})u_1 \times u \tag{2.39}$$

$$t_1 = 4 + \xi^2 (u_1 \times u_2)^2 - \frac{|u|}{b^2} + (\frac{1}{b^2} - \frac{1}{a^2})u_2 \times u \tag{2.40}$$

$$h = t_1 + t_2 - 2 - \frac{\xi^2}{b^2}(u_1 \times u_2) \times u \tag{2.41}$$

$$p = -h \tag{2.42}$$

$$q = t_1 t_2 - 4 \tag{2.43}$$

$$w = 4h - t_1{}^2 - t_2{}^2 \tag{2.44}$$

$$\psi = 4(p^2 - 3q)(q^2 - 3wp) - (9w - pq)^2 \tag{2.45}$$

$$s_1 = h^2 - 2t_1 t_2 - 4 \tag{2.46}$$

$$s_2 = t_1{}^2 t_2{}^2 + 8t_1 t_2 - 2h(t_1{}^2 + t_2{}^2) \tag{2.47}$$

We defined the function ψ as contact function by the relations, through which we evaluate $\psi, s_1, s_2 t_1, t_2$ and h.

$$u_1 = m_1 i + m_2 j + m_3 k \tag{2.48}$$

$$u_2 = l_1 i + l_2 j + l_3 k \tag{2.49}$$

$$u = xi + yj + zk \tag{2.50}$$

$$|u| = \sqrt{x^2 + y^2 + z^2} \tag{2.51}$$

$$u_1 \times u_2 = (m_2 l_3 - m_3 l_2)i + (m_3 l_1 - m_1 l_3)j$$
$$+ (m_1 l_2 - m_2 l_1)k \tag{2.52}$$

$$(u_1 \times u_2)^2 = (m_2 l_3 - m_3 l_2)^2 + (m_3 l_1 - m_1 l_3)^2$$
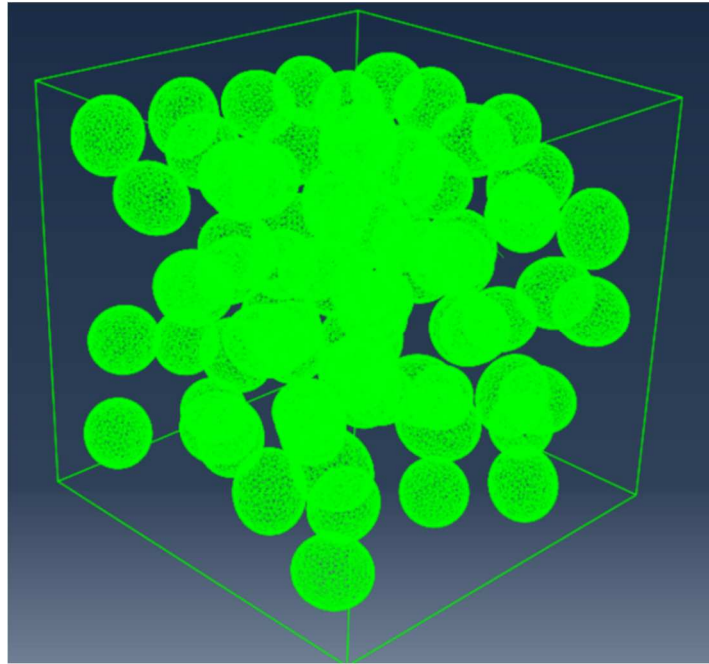$$+ (m_1 l_2 - m_2 l_1)^2 \tag{2.53}$$

$$(u_1 \times u_2) \times u = (m_2 l_3 - m_3 l_2)x + (m_3 l_1 - m_1 l_3)y$$
$$+ (m_1 l_2 - m_2 l_1)z \tag{2.54}$$
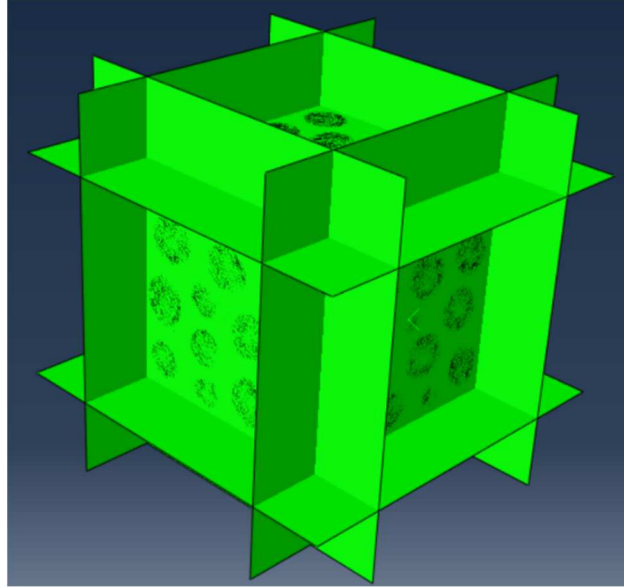
$$u_1 u_2 = m_1 l_1 + m_2 l_2 + m_3 l_3 \tag{2.55}$$

$$u_1 u = m_1 x + m_2 y + m_3 z \tag{2.56}$$

$$u_2 u = l_1 x + l_2 y + l_3 z \tag{2.57}$$

The three-step simulation procedure in our analysis can be presented schematically in Fig. 2.5 (a) (b) (c)
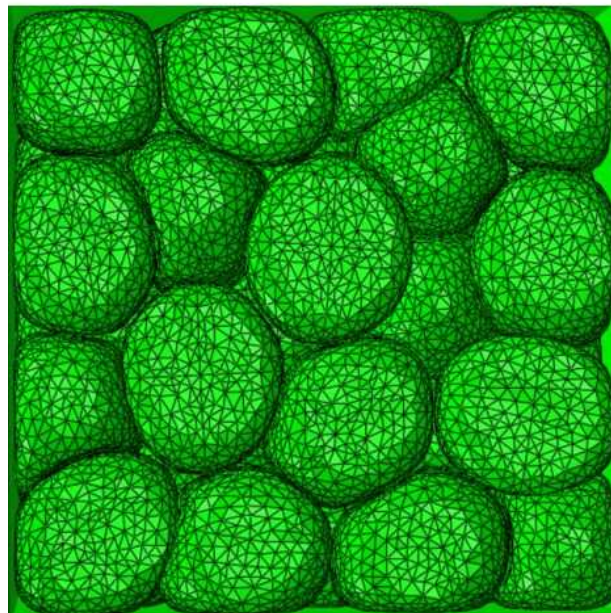

(a)

(b)

(c)

Fig 2. 5 3D finite element model schematically describing the simulation procedure (a) Step 1: dynamic collision algorithms for generating randomly-dispersed, impermeable ellipsoids. (a) Step 2: compression of the system with rigid domain walls (c) Step 3: stead

Chapter Three: Simulation results for Compression Model

3.1 Conduction in Contact Model

The simulated effective conductivity provided by finite element analysis was studied as a function of volume fraction of the inclusions in the contacting system. At the first part of the parametric studies, the particle-particle or particle-container was assumed as a frictionless contact to minimize the possibility of energy dissipation. Also, infinite gap conductance or zero contact resistance was presumed since the simulated effective conductivity is independent of gap conductance as it is approaching infinite and so that is dependent on contact area alone. Fig. 3.1(a)-(d) shows the nodal temperature under specific volume fraction of the inclusions. The nodal temperature field shown in Fig. 3.1(a) as the volume fraction is 30.5%. It can be easily seen that no conductive path is formed under this volume fraction through the system and the effective conductivity is zero, accordingly. In addition, most of the particles are separated from each other and rare deformation is detected across the system. There are two types of nodal temperature fields in this specific volume fraction. The nodal temperature is uniformly distributed with a value of unit for those particles associated with the top domain wall, while zero temperature for those particles connected to the bottom domain wall. As the domain walls continue compressing the system, the volume fraction increases to the level of jamming fraction (or percolation threshold), at least one conductive path is formed under the

current nodal temperature field, as can be seen in Fig. 3.1(b) Although the temperature field at some vertical paths is not uniform, the vertical temperature gradients can still be reflected by the color variations of the clusters.

It can be clearly seen that the particles stay close enough to each other, even most of them have mechanical contact regions with the adjacent pairs when the volume fraction of the particle reaches its jamming fraction or close-packing limit. Fig. 3.1(c) shows the deformable particles contact behavior when the system volume fraction increases to 48.2% during the compression. The contact regions can be clearly seen among the deformed particles and more than one conductive path is formed. Most of the particles are interconnected with each other, and the temperature gradients for each of the conductive paths that vertically cross the system are about the same. When the volume fraction future increases to 93.6% as presented in Fig. 3.1(d), the elastic deformation becomes so significant that the particles can no longer retain their original shapes. The temperature gradients and calculated heat flux among each vertically conductive path are approximately uniformly arranged from the top side to the bottom. The uniformly compressed particles comprise the system as a homogeneous particulate material system.
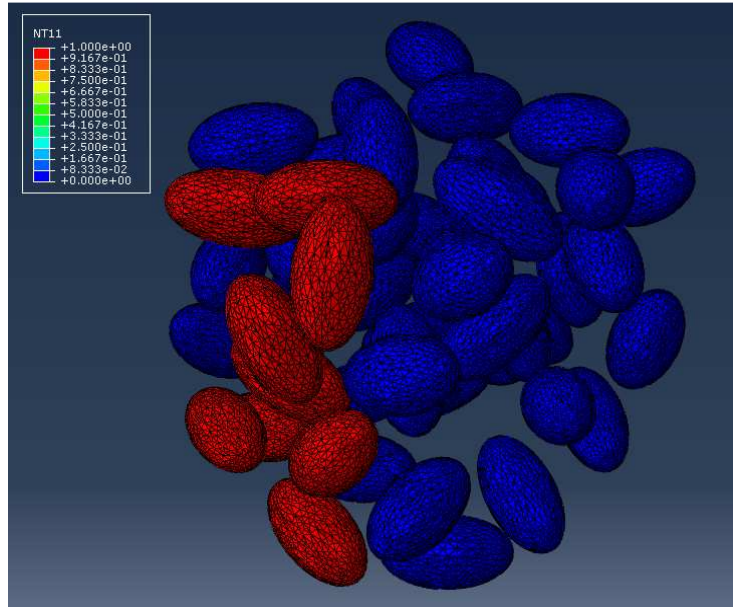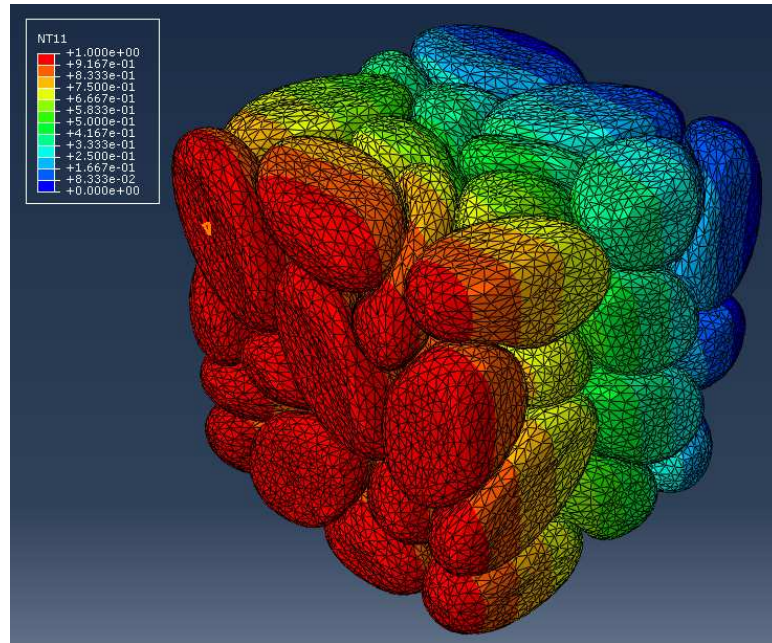
(a)
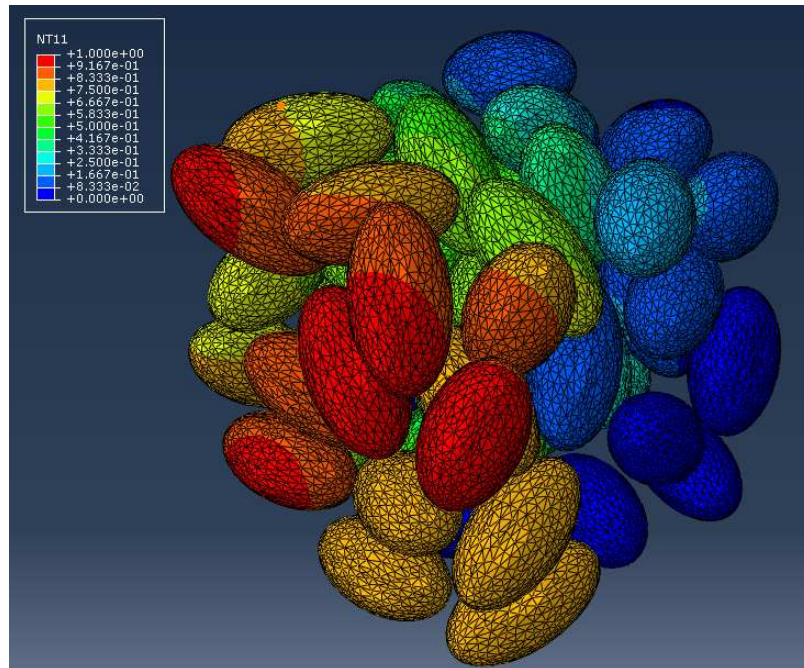
(b)
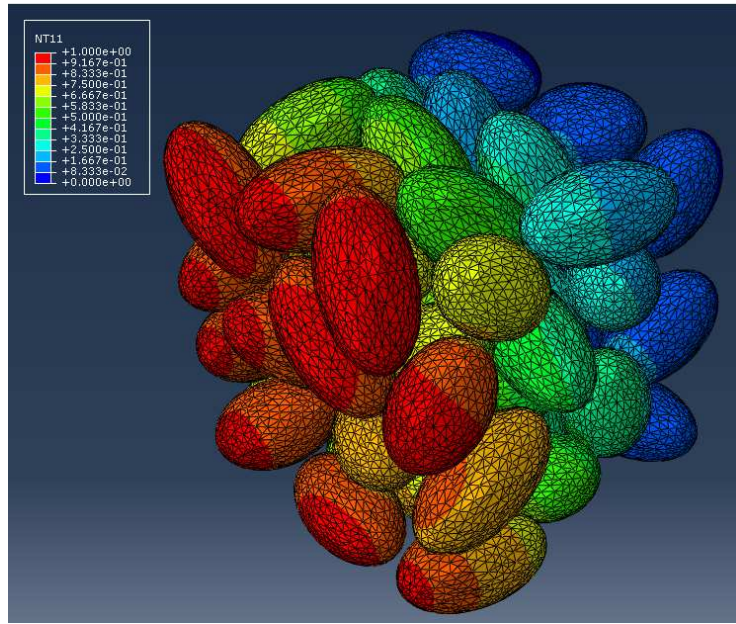
(c)

(d)

Fig 3. 1 Nodal temperature field in the contact model containing the following volume fractions: (a) 30.5%; (a) 40.77%; (c) 48.2%; (c) 93.06%.

3.2 Parametric Study

The chosen of the total number of finite elements on each particle is of importance in our study since it will affect both simulation accuracy and efficiency: the appropriate number of finite elements must be simulated in order to accurately describe the feature of particle interfaces, however, the computational time will increase exponentially as the increasing of finite elements on particles. Thus, in our study, we constructed a convergence study at the beginning to investigate the sensitivity of the solution with respect to the mesh densities, so that we can obtain the balance between simulation accuracy and efficiency. The outcomes show that 618 nodes and 1232 elements meshing on each particle could ensure the numerical efficiency as well as accuracy in our cases.

3.2.1 The effect of particle numbers on conductivity

The effective conductivity was studied as a function of volume fraction of the particulate system. Fig. 3.2 shows a relation of simulated effective conductivity achieved through three different cases: (1) 120 spheres with the radius of 0.07 (2) 250 spheres with the radius of 0.055 (3) 300 spheres with the radius of 0.0516. In this study, we defined a dimensionless conductivity, shown in Fig. 3.2 for example, in which it is normalized by the parameters describing the conductivity of particulate material as shown

$$K = \frac{K_{sys}}{K_{particle}} \tag{3.1}$$

Where K_{sys} describes the conductivity of the entire system, $K_{particle}$ represents the conductivity of particulate material. The calculated value K is dimensionless since

K_{sys} and $K_{particle}$ have the same unit. It can be seen from the relations that the contact model in all three cases starts to have non-zero conductivity value when the volume fraction is above a certain threshold, which is located between 32%-35% in terms of volume fraction. Below that certain threshold, zero conductivity was obtained since there is no conductive path formed along the temperature distribution. Reaching this stage of the compression process, the system is considered to be "jammed" and the particles are starting to be in full contact with each other. It is clear that the percolation thresholds for the three cases here are nearly the same. This can be explained as no energy dissipation caused in the system and the radius reduces as the number increases in order to keep consistent volume fraction at the same time for all three cases. Above the percolation threshold, the effective conductivity is almost a non-linear function of the system volume fraction. For example, the effective conductivity increased by 367% at 80% volume fraction compared to 40% volume fraction. At the range of 35%-60% volume fraction, the simulated results oscillate irregularly as the volume fraction increases. It is related to the reason that the contact pairs do not contact against each other tightly so that there still exist some void spaces for them to adjust their locations, although they have already begun to contact with each other at this volume fraction. The alteration of contact regions irregularly lead to the fluctuation of conductivity since the contact area is the only factor in deciding conductivity under infinite gap conductance assumptions. As the volume fraction increased to 65%, it is seen that the simulated results do not have much difference for the three different cases. This is because the particles were in contact against each other tightly, in which the void spaces were rare and the particle spatial locations variations were limited. The limitations in contact region variations lead to the

constant value of effective conductivity. In conclusion, the simulation results do not show much difference among the different size or number of particles.

3.2.2 The effect of particle shape on conductivity

This study works to make a comparison of conductivity among the spherical inclusions and ellipsoidal inclusions. The simulation results with errorbar, which involve mean values and standard variations, are presented in Fig. 3.3 Two separate cases are implemented here: (1) 120 spheres of radius 0.07 (2) 120 ellipsoids of semi-axis lengths 0.147, 0.049, 0.049 in x, y, z directions, respectively. The estimated value of percolation threshold for the different shape of inclusions is similar, as 31% in terms of volume fraction. However, this value is not consistent with the theoretical prediction due to the scaling effect induced by a relatively small number of inclusions investigated here. The simulated results do not differ too much for the different shape of inclusions when the volume fraction is below 70% due to the relatively small number of particles investigated here. The geometry characteristic of the particles does not play an essential role, although the variations in conductivity are discernable. However, the results deviate slightly and even the difference between the two types of inclusions exceed each one's deviation limit when the volume fraction reaches 75%. This can be explained as the distinct geometry characteristic of two different inclusions lead to the difference in contacting regions under the compression process. Another benefit for adding errorbar to the results is that the curves could become smoother. The polynomial equations that describe the relation of conductivity and volume fraction of the current two cases can be achieved by using the

least square method through embedded function in MATLAB®. The polynomial equation for the ellipsoidal system can be presented as

$$Y = 5.1702x^0 - 1.1617x^1 + 1.089x^2 - 0.0056x^3 + 0.0002x^4 \qquad (3.2)$$

The polynomial equation for the spherical system can be presented as

$$Y = 0.983x^0 - 0.3765x^1 + 0.0467x^2 - 0.0028x^3 + 0.0001x^4 \qquad (3.3)$$

The data fitting method for the ellipsoidal system or spherical system can be depicted in the Fig. 3.4 and Fig. 3.5, respectively.
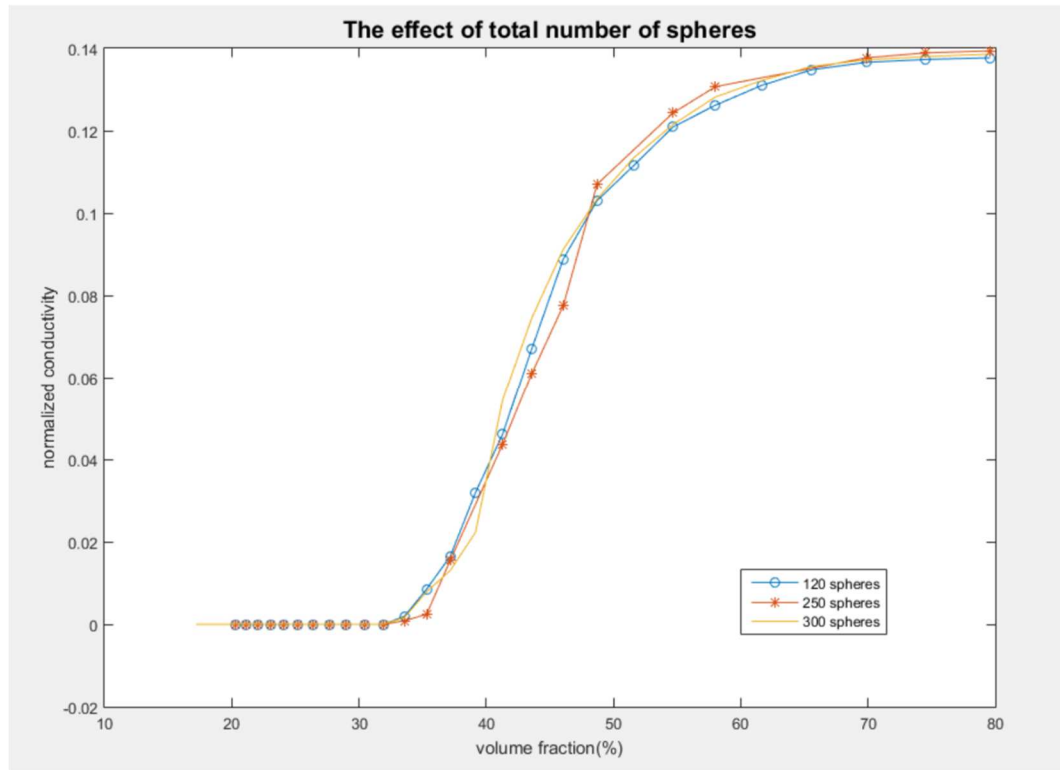

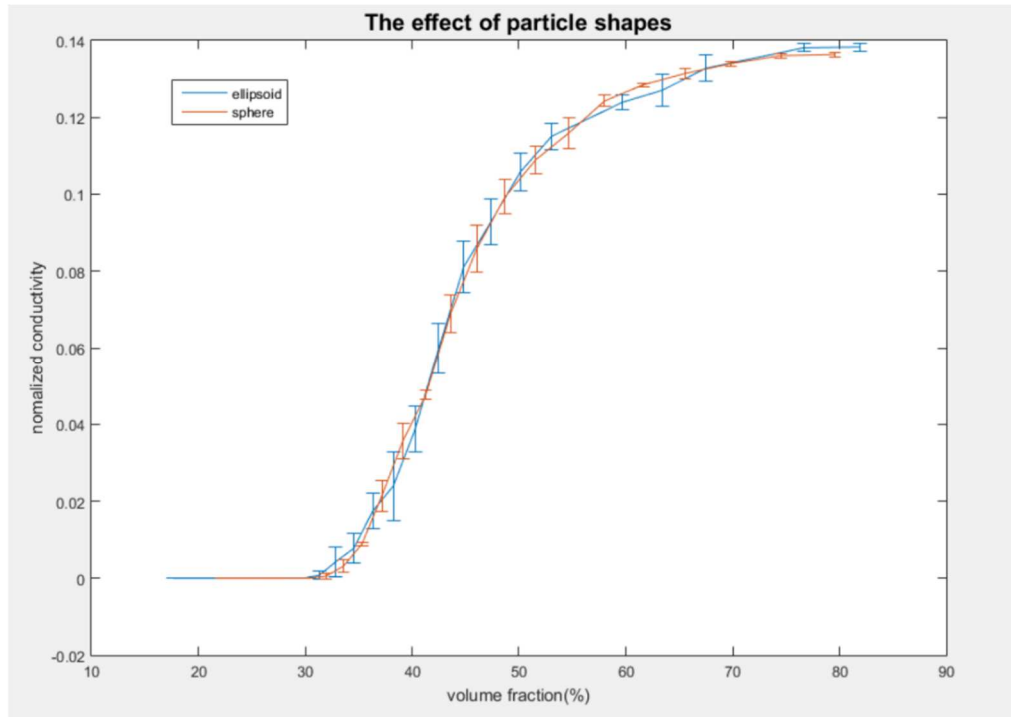Fig 3. 2 The effect of the particle number on conductivity

54
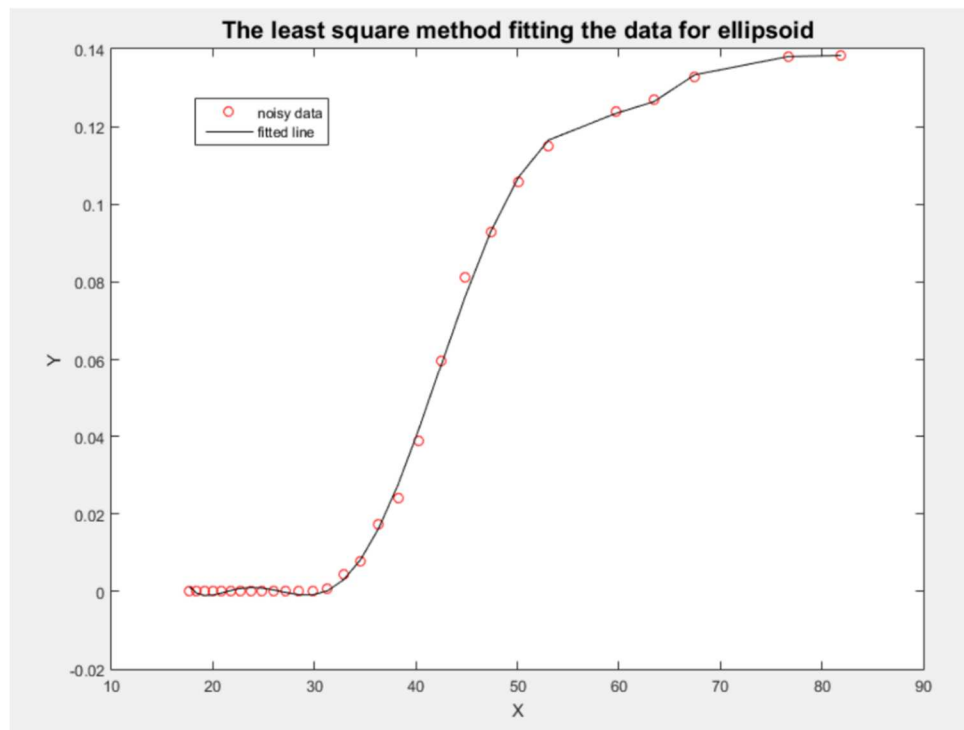
Fig 3. 3 The effect of particle shape on conductivity

Fig 3. 4 Data-fitting methods for ellipsoidal system
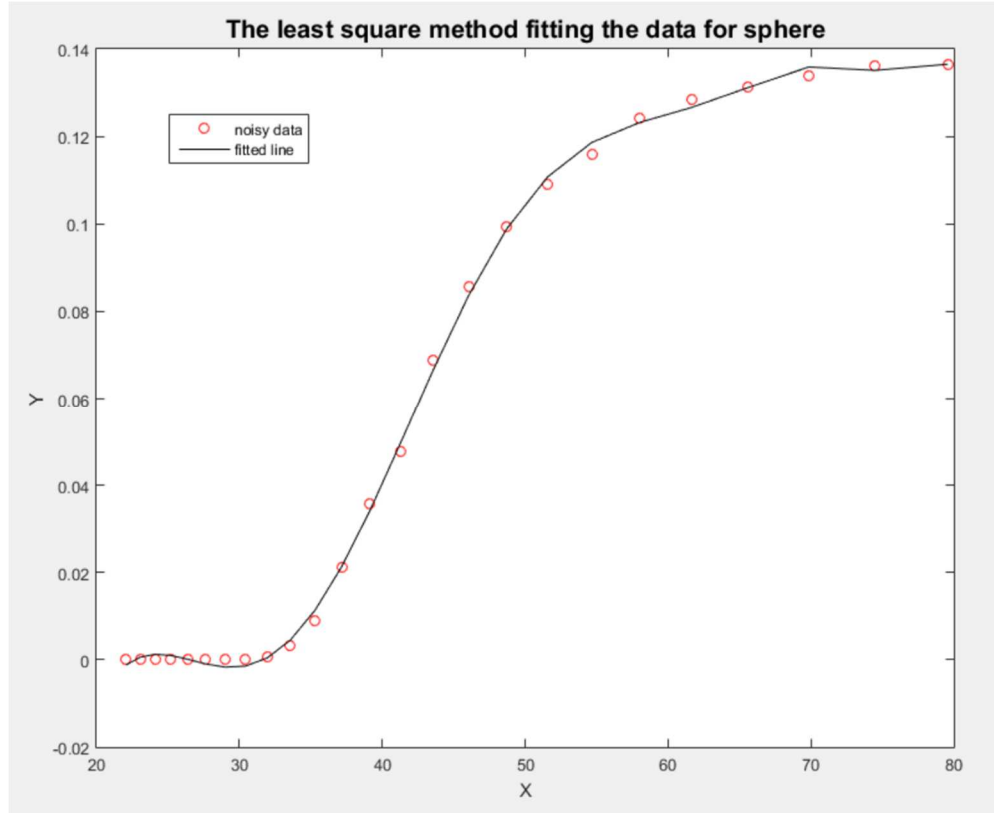
Fig 3. 5 Data-fitting methods for spherical system

3.2.3 The effect of randomness distribution of ellipsoids on conductivity

The randomness distribution of ellipsoids refers to the randomly-generated center-point location and orientation angles in x, y, and z directions. In this study, a case of 120 ellipsoids of semi-axis 0.147 0.049 0.049 in x, y, z directions, respectively, was run three times to obtain the randomly-distributed ellipsoidal inclusions and then make a comparison of conductivity under the same volume fraction in three cases. The plot of simulated results was shown in Fig. 3.6 that as a non-linear function of the volume fraction. As expected, the estimated percolation threshold agrees well with each other in three cases since the same ellipsoids were assumed. Additionally, the curves start to

56

experience irregular oscillations due to the variations in contact regions among particles. The amplitude of conductivity within this range of volume fraction is dependent on the hardness of particles, which is determined by Young's Modulus and Poisson's ratio. The amplitude of conductivity increases significantly as the particles become harder. As the volume fraction increases up to 70% and the spaces for particles location adjustment becomes limited, the simulated conductivity for these randomly-distributed particles tend to get closer since the effects of randomness of location were terminated when the particles contacted against each other tightly. We can obtain the mean value and standard derivations for the conductivity in three cases and get a smoother curve shown in Fig. 3.7.

3.2.4 The effect of the hardness of particles on conductivity

To study the effects of the hardness of particles on the overall conductivity, we performed finite element analysis by altering the value of Young's Modulus while fixing the value of Poisson's ratio to 0.495. Three same systems of particles were maintained, and the Young's Modulus was the only variable (1) 120 sphere of radius 0.07 with Young's Modulus value of 10 (2) 120 sphere of radius 0.07 with Young's Modulus value of 1

(3) 120 sphere of radius 0.07 with Young's Modulus value of 0.1. The simulated results were shown in Fig. 3.8 All three simulation results show a relative well agreement with each other, especially when the volume fraction is higher than 50% since the limitation of the effects of particle hardness under the rare space left for location adjustment. The amplitude of oscillations in the conductivity is larger of the material containing harder particles or particles with higher Young's Modulus compared to the soft

one. The reactive force between contacting particles, which is responsible for the initial velocity of particles after collisions, was supplied by the intermittent, dynamic collisions among particle-particle or particle-wall. The reactive force among particles might be larger for those of harder interfaces compared to the "softer" one, implying there are more frequent changes of contact regions that occurred in the harder one. Thus the results of soft particles look relatively smooth. The clearer comparison can be seen in Fig. 3.9 in which a harder particle with 150 value of Young's Modulus was investigated while the other of same parameters was maintained. The oscillations in results of harder particles are more obvious, although the two distinct systems reach almost the same value of conductivity when the volume fraction is sufficiently high. Another point that needs to be mentioned is that the material system containing soft particles can reduce the percolation threshold. For example, the particulate system with Young's Modulus of 1 or 0.1 has a reduction of 5% in volume fraction in comparison with the system of 10 value of Young's Modulus. This can be explained by the presence of reactive force between particles, which can be regarded as a propulsion to provide velocity for collisions, could facilitate the particle adjustment.
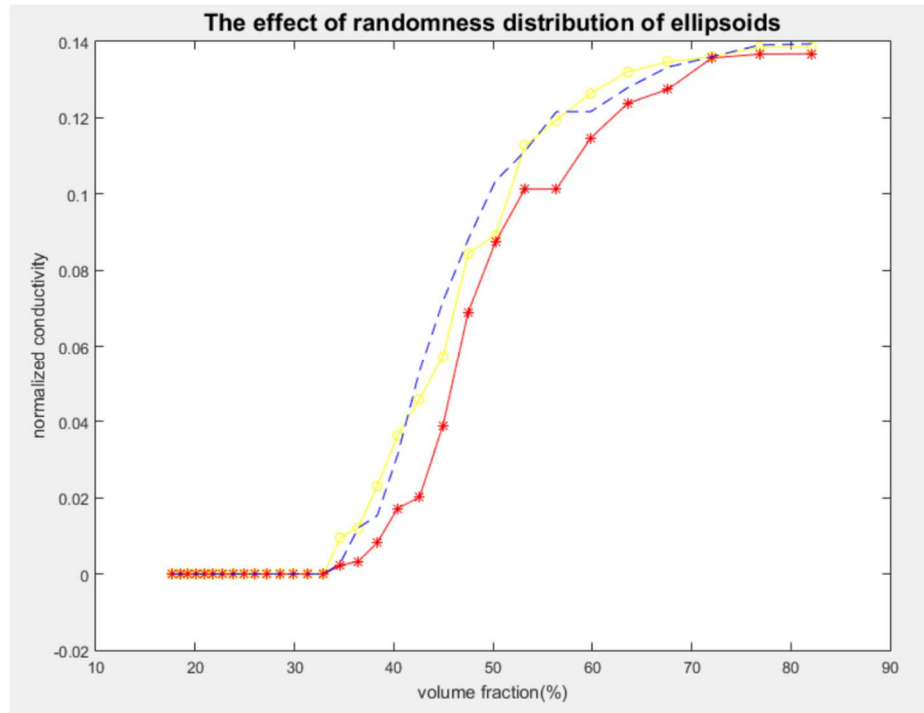
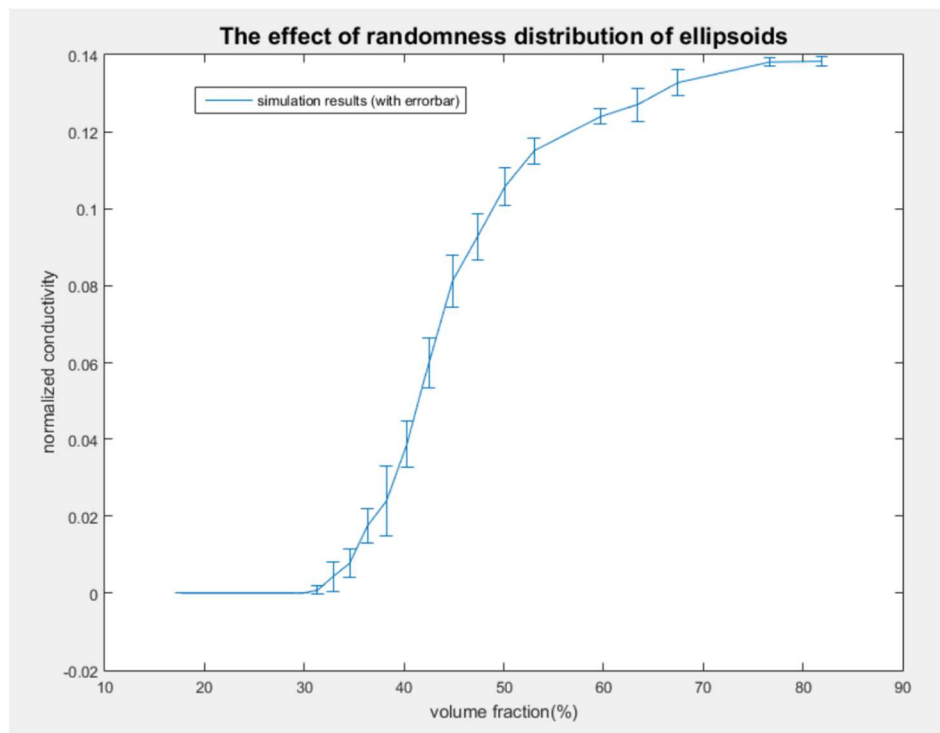Fig 3. 6 The effect of random-distribution of ellipsoids on conductivity

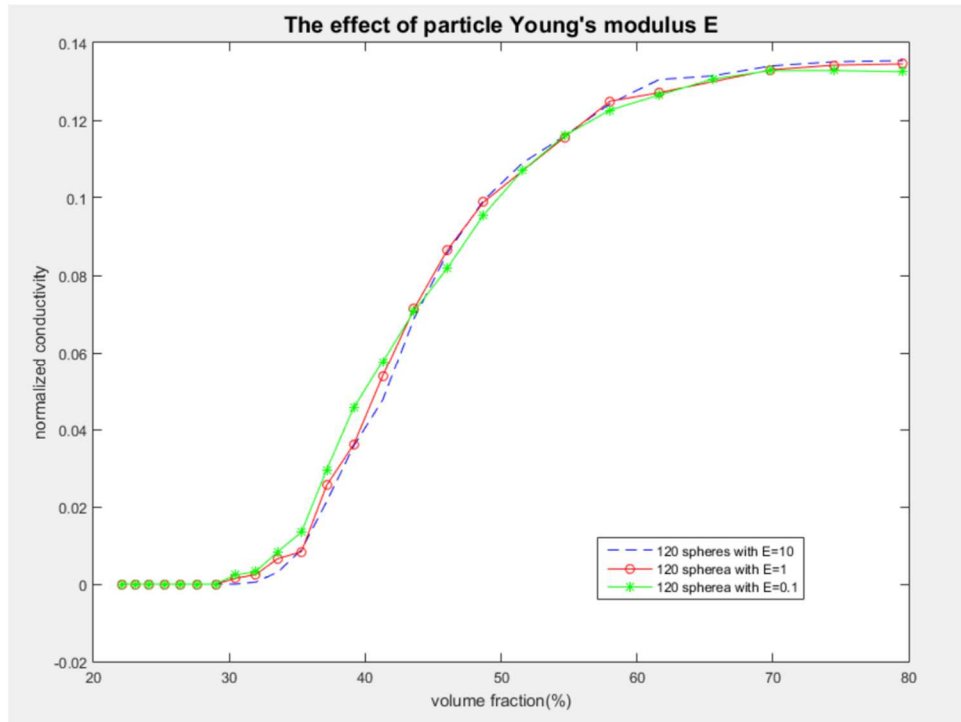Fig 3. 7 The effect of random-distribution of ellipsoids on conductivity (with errorbar)

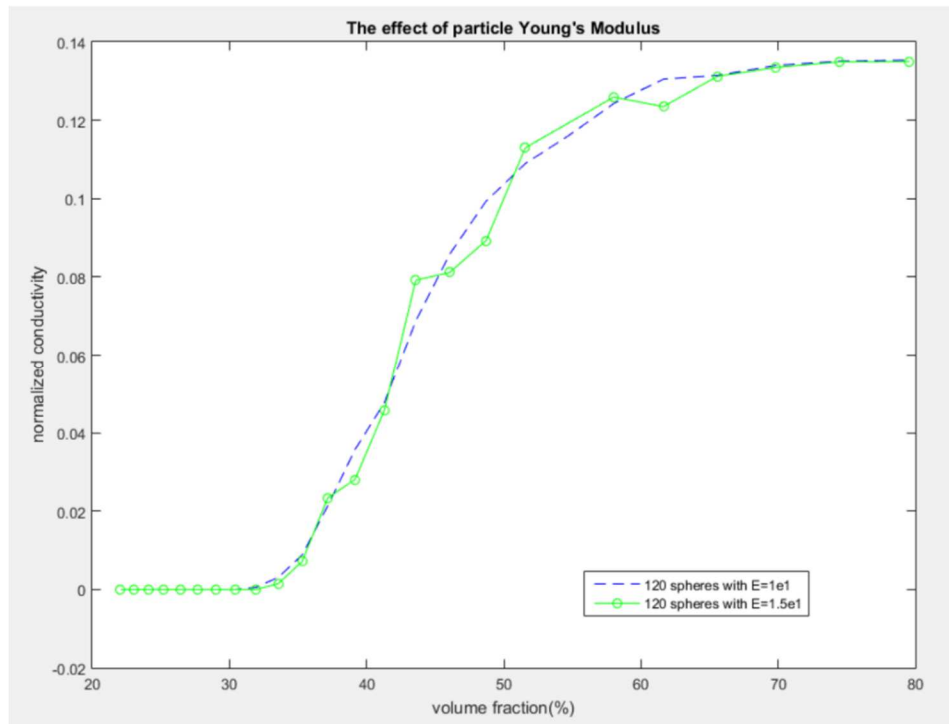Fig 3. 8 The effect of the hardness of particle on conductivity

Fig 3. 9 The effect of the hardness of particle on conductivity

60

3.2.5 The effect of ellipsoid aspect ratio on conductivity

The ellipsoid aspect ratio, ε, defined as the ratio of the major half-axes length to the minor half-axes length, is a significant parameter that was related to describing the micro- or macro-structure of a material system in many literature works. The geometry used in this study is assumed to be a prolate spheroid, in which the length of two minor axes is equal to each other. Three distinct cases with aspect ratio as equal to 1, 3, and 6 investigated here, respectively, with parameters as (1) 120 prolate spheroids of radius 0.07 (2) 110 prolate spheroids of semi-axis lengths 0.15, 0.05, 0.05 (3) 107 prolate spheroids of semi-axis lengths 0.24, 0.04, 0.04. The chosen number of ellipsoids and semi-axis lengths are based on the consistency of volume fraction under a compression process. The simulated results are shown in Fig. 3.10, in which the effective conductivity is a function of the ellipsoid aspect ratio. Specifically, the effective conductivity decreases with the ellipsoid aspect ratio as the same volume fraction assumed. However, the results start to deviate from each other since the volume fraction is above the percolation threshold, which is located at around 30%. The difference increases as the volume fraction increases and it is expected to be a significant discrepancy when the volume fraction is sufficiently high. For example, the effective conductivity of the material system with an aspect ratio equal to 1 is 3.8% higher than that of the system with an aspect ratio equal to 3 and 8% higher than that of the system with an aspect ratio equal to 6, at the volume fraction of 80%. Also, it can be detected that the results in the material system with an aspect ratio equal to 1 experience rare oscillation compared to the other

two. This is because of the geometry characteristic of a sphere that leads to the regular of contact regions.

3.2.6 The effect of ellipsoid shapes on conductivity

The three types of ellipsoidal inclusions, which are tri-axial ellipsoid, oblate spheroid, and prolate spheroid, were investigated in this study to figure out the effects of ellipsoid shapes on effective conductivity. The parameters used in these three cases are (1) 83 ellipsoids with semi-axis lengths of 0.16, 0.08, 0.04 (2) 71 ellipsoids with semi-axis lengths of 0.1, 0.1, 0.06 (3) 98 ellipsoids with semi-axis lengths of 0.06, 0.06, 0.12. The simulated results for impermeable ellipsoidal inclusions that are tri-axis, oblate or prolate are shown in Fig. 3.11, in which the effective conductivity varies with different ellipsoid shapes. It can be seen that the conductivity of three distinct systems has close correlations with lower values of volume fraction. However, they start to deviate from each other as the volume fraction is around 50%. The difference increases as the volume fraction increases and it is expected to be a significant discrepancy when the volume fraction is sufficiently high. In addition, the conductivity of the prolate spheroidal system is higher than that of the oblate spheroidal system and tri-axial ellipsoidal system. For example, the effective conductivity of the prolate spheroidal system is 8.7% higher than that of the oblate spheroidal system and 36.3% higher than that of the tri-axial ellipsoidal system, at the volume fraction of 82%. The distinct geometry characteristic of each ellipsoidal system results in the difference of contact regions under the compression process and thus affects the overall conductivity especially when the particles are contacted tightly against each other or the volume fraction of the system is sufficiently high. The contact situation

can be estimated from the Fig. 3.12, Fig. 3.13, and Fig. 3.14, which exhibits the three distinct morphological shape of the inclusions.
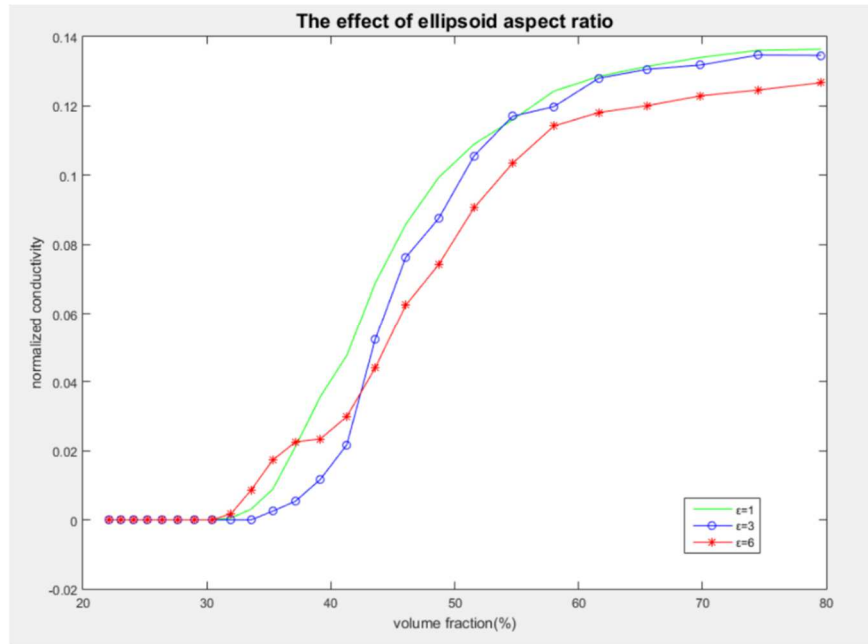

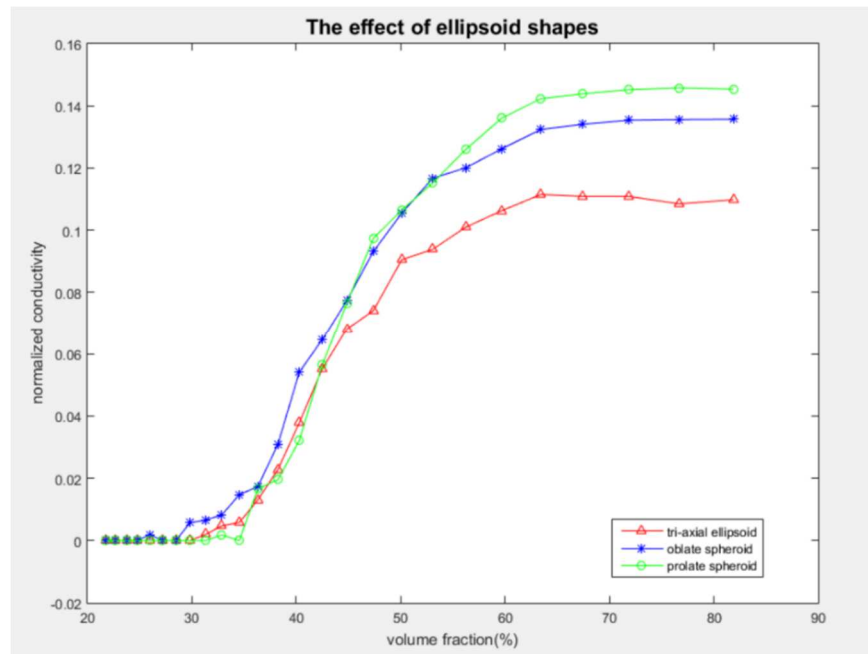Fig 3. 10 The effect of particle aspect ratio on conductivity

Fig 3. 11 The effect of the morphological shape of the inclusions on conductivity
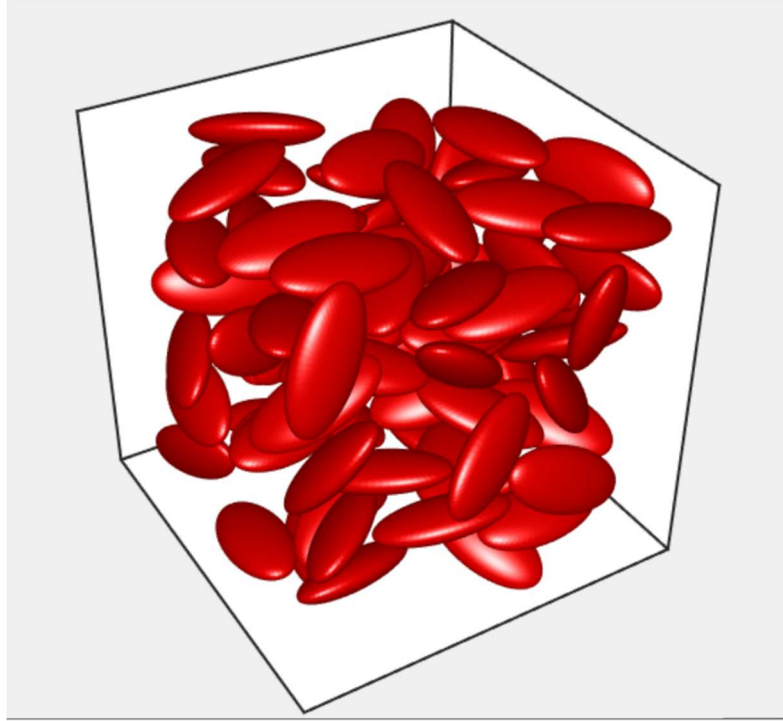
Fig 3. 12 The visualization of tri-axial ellipsoidal inclusions
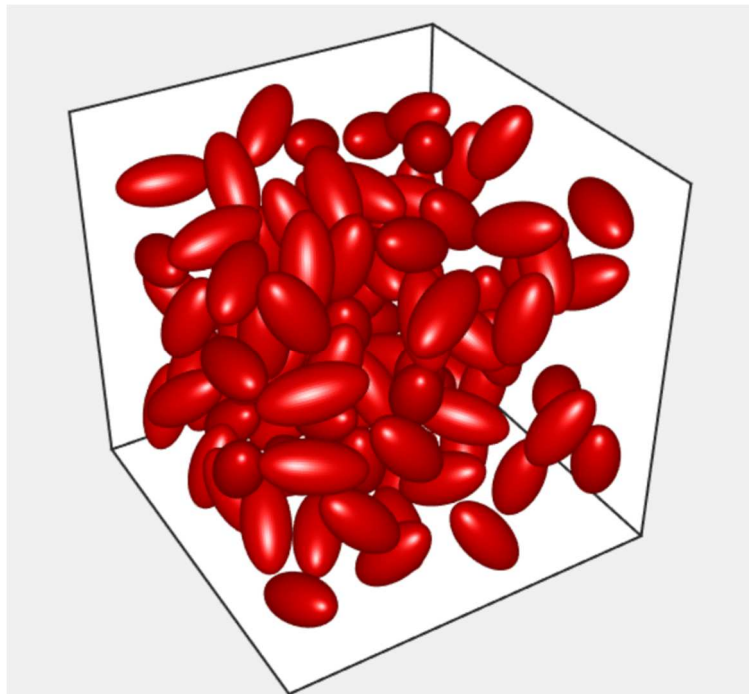
Fig 3. 13 The visualization of prolate spheroidal inclusions
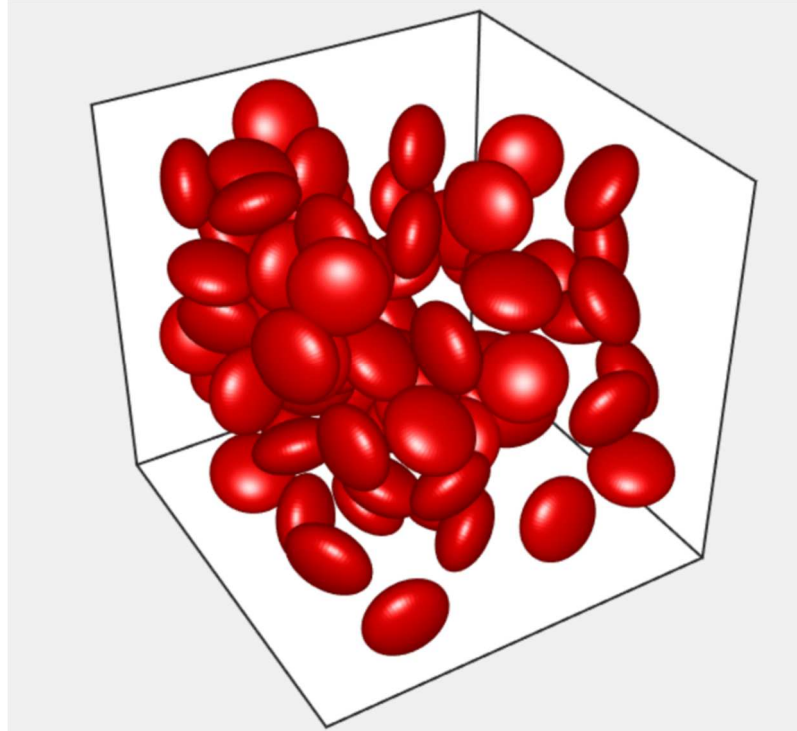
Fig 3. 14 The visualization of oblate spheroidal inclusions

3.2.7 The effect of inter-particle friction on conductivity

The above works were based on the assumption of frictionless contact, in which the alteration in contact area is the only factor that could change the overall conductivity. Incorporation of realistic, mechanical deformations, which will result in rough or permeable surfaces, are unavoidable during the compression processes in manufacturing. Therefore, in this part of the parametric study, the above works will be extended to involve in inter-particle or particle-container friction effects, which are considered to be able to represent a more realistic particulate material system.

A quantitative relation has been established between the conductivity and volume fraction in the following five cases (1) 120 spheres of radius 0.07 with zero value of

friction coefficient (2) 120 spheres of radius 0.07 with 0.15 value of friction coefficient (3) 120 spheres of radius 0.07 with 0.3 value of friction coefficient (4) 120 spheres of radius 0.07 with 0.5 value of friction coefficient (5) 120 spheres of radius 0.07 with 0.9 value of friction coefficient. No further contact behavior was monitored for friction coefficient value greater than 1, since the particles were believed to be "sticky" enough when the friction coefficient is around 1. In Figure. 3.15, we can detect that the sudden increase occurred on the conductivity when the system volume fraction reaches its percolation threshold. The values of percolation threshold differ in these five cases, more specifically, the presence of inter-particle friction could lower the value of percolation threshold. Since the existence of inter-particle friction could interfere the location adjustment of particles, implying that the more flexible and rapid changes occurred in the contact area for particles with frictionless contact when some void spaces left in the system. For example, a friction coefficient value of 0.15 will reduce the percolation threshold from 34% to 32%, in terms of volume fraction. A friction coefficient value of 0.3 will reduce the percolation threshold from 34% to 31%. A friction coefficient value of 0.5 will have the reduction of percolation threshold further extend to 30%, in terms of the volume fraction of non-friction contact model. The maximum reduction 5% will occur when the value of friction coefficient is 0.9, which is believed to be higher enough to make the particles "sticky". Above the percolation threshold, the effective conductivity increases as a non-linear function of volume fraction of particles. In Fig. 3.15, it seems that the values of conductivity experience oscillations during the compression processes. Since the frictionless contact won't impede the particle adjustment under certain volume fraction, leading to the rapid changes of contact regions among particles. Whereas, the system will

have energy dissipation under the presence of friction, which would reduce the oscillations in the resulting conductivity and lead to the smoother looking of the curves. It can also be detected that the conductivity of frictionless contact model is lower than that of the friction contact model when the volume fraction is between 40%-55%. This is because the location changes are limited in friction involved contact model, which will lead to larger contact regions compared to those who are free to move. When the compression processes continue and the volume fraction is exceeding 60%, all the five curves become flatten since the variations in contact area are limited as the void space in the system is rare. The difference between these five is discernable, but not quite significant. It can be seen that the conductivity decreases for higher friction coefficient under the same volume fraction. The normal stresses among particles are resulting from local deformation of particles in the jammed system and the magnitude of normal stress increases as the compression process continue. The shear force is proportional to the friction coefficient and normal stress in friction contact model as mentioned above and the particles start to have relative movement when the shear force increases to the critical value. Thus, the contact model with higher friction coefficient is more likely to have relative movements among particles as the volume fraction exceeds 60% in this study. Consequently, the reduced contact area in higher friction coefficient case will lead to a reduction in corresponding conductivity. The overall shapes of the non-linear curves are dependent on the conductivity of the particulate material and the inter-particle friction. The fluctuant behavior in frictionless contact model can be improved by adding the mean values and the standard deviations, as presented in Fig. 3.16. It can be seen that the

standard deviations vary with the volume fraction, the uncertainties in conductivity are relatively larger when the volume fraction reaches 40%-50%.

3.2.8 The effect of particle-container friction on conductivity

This study determines the relations between the conductivity and volume fraction involving the particle-container friction effects. Fig. 3.17 shows a plot of simulated effective conductivity obtained from the finite element analysis in the following five cases (1) 120 spheres of radius 0.07 with zero value of particle-container friction (2) 120 spheres of radius 0.07 with 0.15 value of particle-container friction (3) 120 spheres of radius 0.07 with 0.3 value of particle-container friction (4) 120 spheres of radius 0.07 with 0.5 value of particle-container friction (5) 120 spheres of radius 0.07 with 0.9 value of particle-container friction. The results in this study have a similar pattern compared with the inter-particle friction cases. Likely, the presence of particle-container friction will lower the percolation threshold due to the impediment of particle location adjustment, although the effects are not as significant as that in the inter-particle friction cases. Above the percolation threshold, the conductivity in frictionless contact model is lower compared with that in the friction involved model. This is due to the reasons that the existence of particle-container friction would let the particles get closer with each other, which would result in more contact area and lead to the increases in the value of conductivity. And the oscillation behavior in frictionless contact model, which is resulting from the rapid changes of the contact area, would be relieved by computing mean values and standard variations as shown in Fig.3.18. The slight difference in conductivity can be detected when the volume fraction exceeds 60% due to the implement of

particle-container friction. It is believed that the effect of particle-container friction might be more discernable when ellipsoidal inclusions are involved due to the differences in the geometric property.

3.2.9 The effect of gap conductance on conductivity

All the above discussions were based on the assumptions of infinite gap conductance or zero contact resistance, in which the alteration of contact area is the only factor that could affect the overall conductivity. In the real material system, the contact resistance could be inevitable due to the rough surfaces of particles caused by the compression or mixing processes. Thus in this part, finite gap conductance or nonzero contact resistance was involved and we quantify the relation between gap conductance and effective conductivity of the system.

A special case involved 120 spheres of radius 0.07 with gap conductance as the only variable that varies from 10^0 to 10^6 was studied and quantified. The results shown in Fig.3.19 and Fig. 3.20 present the relation of gap conductance and conductivity when the volume fraction is 80%. Clearly as expected, the gap conductance will definitely lower the effective conductivity as the results start to deviate from each other. And when the volume fraction is sufficient high, the difference could be significant. The results   tell us that the conductivity is independent of gap conductance when it exceeds the value of 10^3 and the conductivity is almost zero when the gap conductance is relatively small. For example, the value of conductivity is 0.03 under the gap conductance of 10^0, which decreased by 333% compared with the situation assuming infinite gap conductance. Also

the nonlinear shape of the curve   is resulting from the both effects of the conductivity of particle material and the contact resistance.

Fig 3. 15 The effect of inter-particle friction on effective conductivity

Fig 3. 16 The effect of inter-particle friction on effective conductivity(with errorbar)
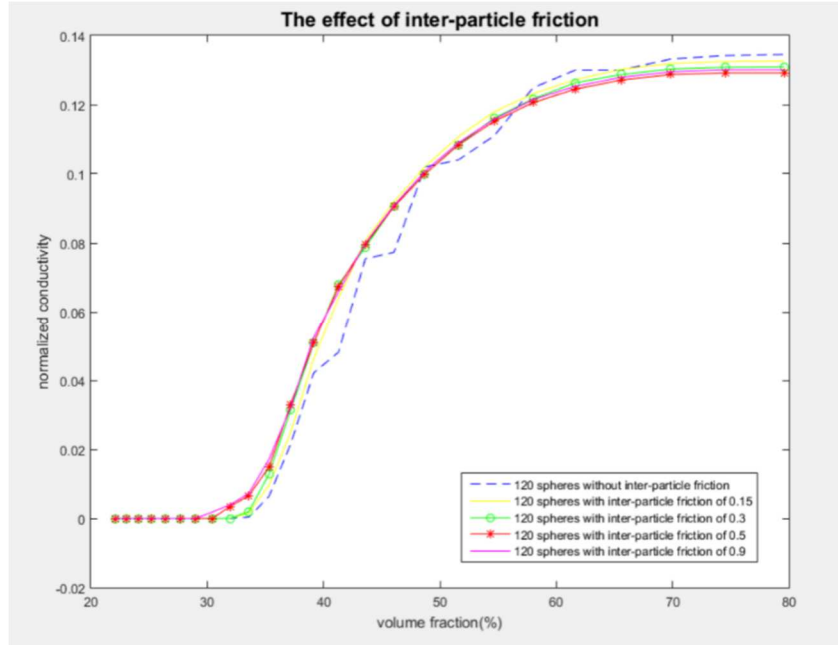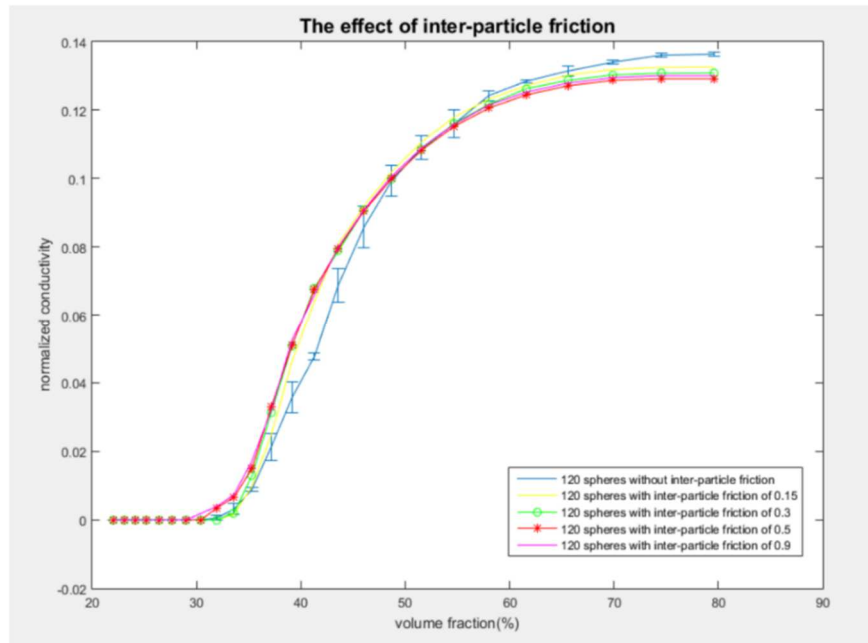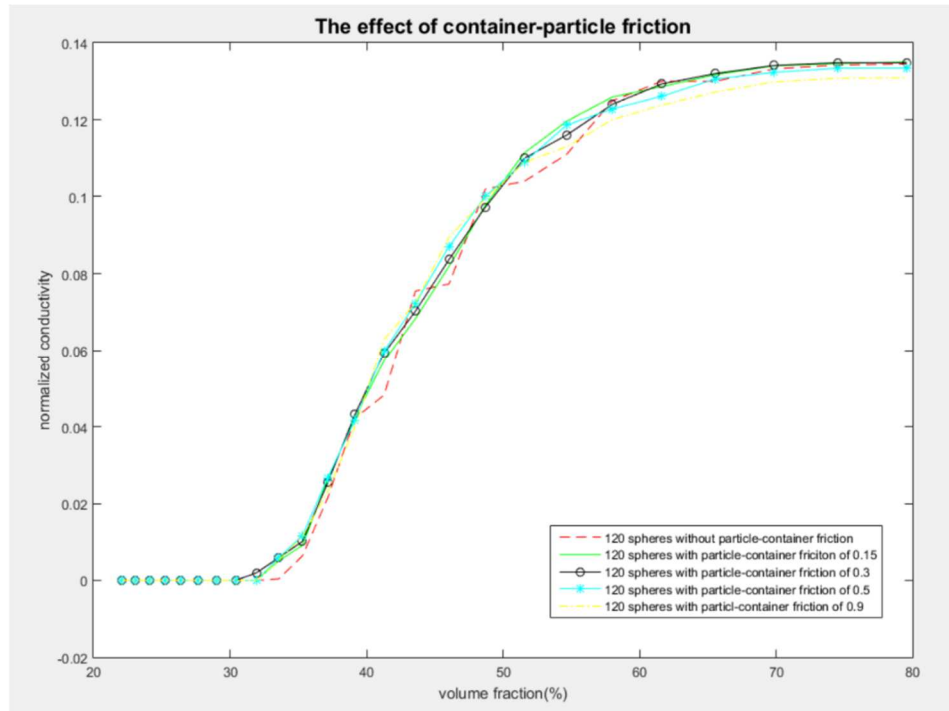
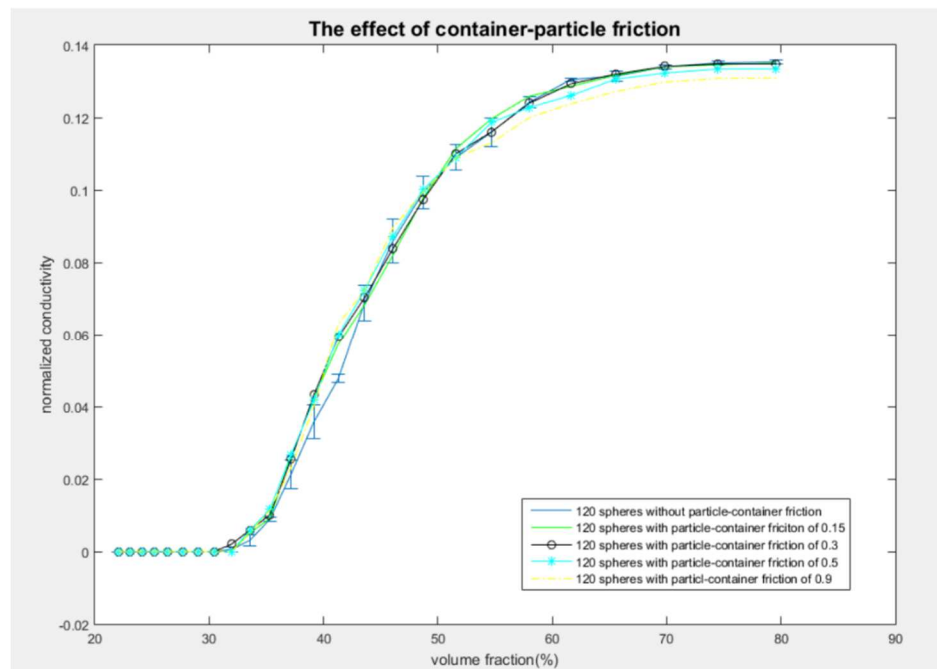Fig 3. 17 The effect of container-particle friction on effective conductivity

Fig 3. 18 The effect of container-particle friction on effective conductivity (with errorbar)
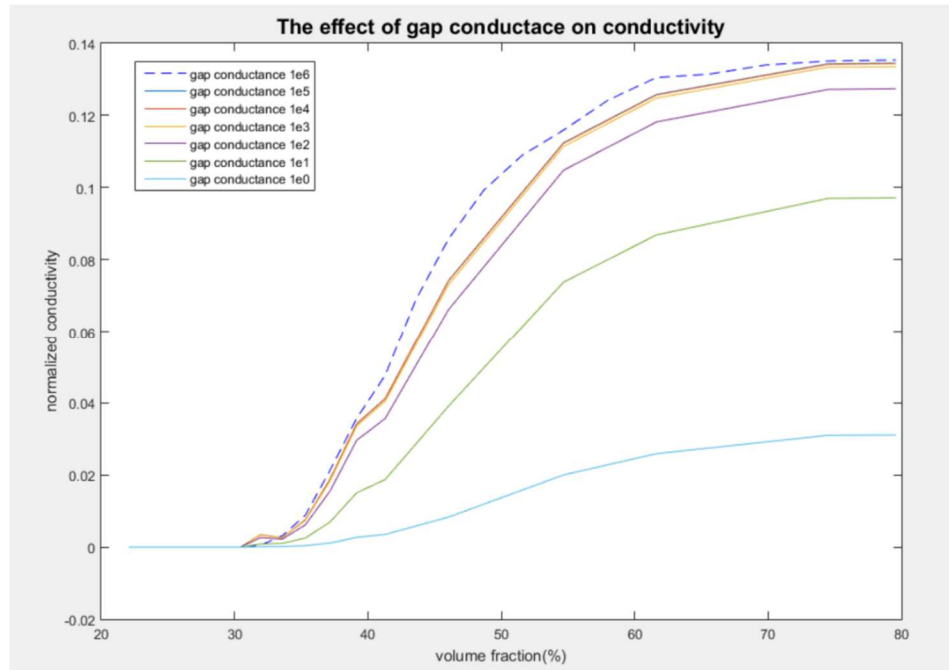
Fig 3. 19 The effect of gap conductance on effective conductivity
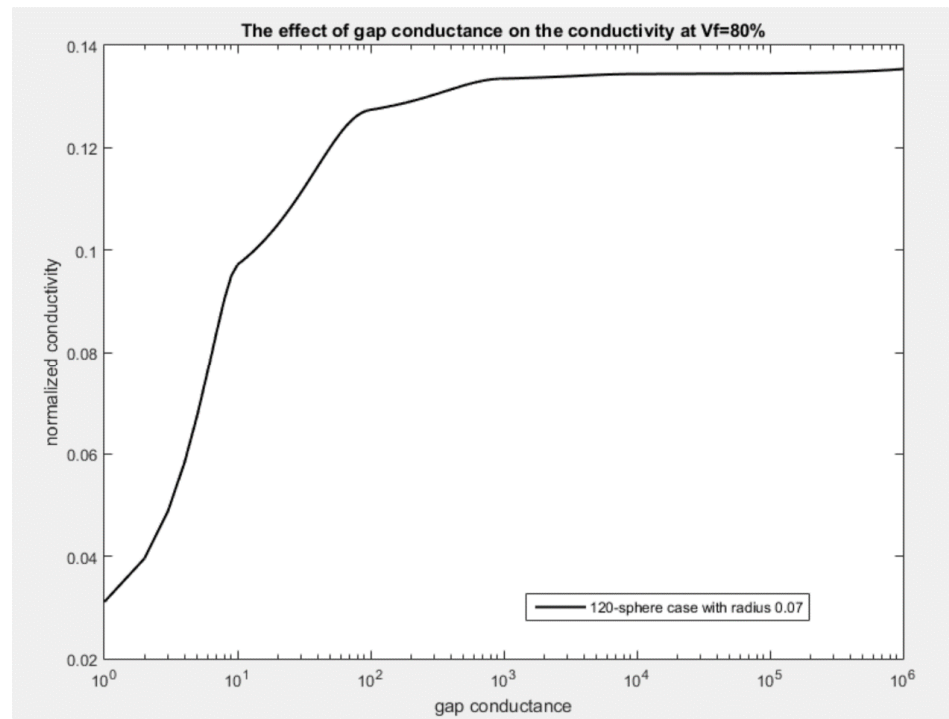
Fig 3. 20 Effective conductivity as a function of gap conductance at volume fraction of 80%

Chapter Four: Conclusions and Future Work

4.1 Conclusions

In this study, a dynamic collision algorithm was successfully developed and efficiently worked in generating randomly-arranged, impermeable, and equisized ellipsoidal or spherical inclusions. The effective thermal or electrical conductivity of the compression model was simulated based on the computational algorithms (i.e. Monte Carlo method) and the finite element method. The overall conductivity was equal to the reactive heat flux of the system cubic with a unit temperature difference across the domain. The effective conductivity has quantitative relations over the effecting factors such as the volume fraction of particles, the particle density over the entire system, the randomness distribution of ellipsoidal inclusions, the interfacial friction, and the contact resistance among particle interface. The contact among deformable particles included not only the basic contact mechanics but also the interfacial friction and contact resistance across the particle-particle interface. Several parametric conclusions have been demonstrated from this study as follows:

(1) The effective conductivity stays at zero for relatively low volume fraction of particles as the system particles are separated from each other with no inter-particle contact, while the conductivity starts to increases over the volume fraction when it reach

(2) Percolation threshold with the particles interconnected. When the volume fraction is sufficiently high, the results reach a plateau due to the limitation in movement of the jammed particles. Also, the temperature gradient and calculated heat flux among each vertical conductive path are almost uniformly distributed from top to bottom.

(3) The mesh density, which strongly affects the simulation accuracy and efficiency, is determined through a mesh convergence study. It is demonstrated that a single particle with 628 nodes and 1232 triangular elements will obtain the balance between computational accuracy as well as efficiency.

(4) A quantitative relation has been obtained from the volume fraction and the effective conductivity for different numbers of particles. The percolation threshold does not vary among these cases due to the fact that there is no energy dissipation in the system with the absence of interfacial friction or infinite gap conductance. The conductivity curve oscillates irregularly as the volume fraction of particles vary from 35% to 60% because the rapid change in contacting area among particles while they are experiencing location adjustment. The conductivity of all these cases reaches a same value of plateau due to the limitations in contact region variations.

(5) The geometry characteristics of particles do not play an essential role in effecting the overall effective conductivity as the volume fraction is below 70%, although small variations are still discernable. However, as the compression pressure continues exerting on the system and the volume fraction is increasing to sufficiently high, the results deviate slightly due to the difference in contacting area of two distinct particles having their own geometric characteristics.

(6) The randomness distribution of the particles can affect particle location adjustment especially when the volume fraction lies between 35% and 70%. The slight difference value of conductivity in the range is account for the irregular change in contact regions among particles.

(7) Hardness effects cannot be neglect during the whole compression process. The conductivity plot oscillates severely containing "hard" particles over the "soft" one. The reactive force among particles, which is responsible for the alterations in velocities after collisions, is larger for the "hard" particle collisions. These reactive forces result in the rapid alterations of contacting regions and thus effective conductivity. Also, the reactive force serve as a facilitate of the particle adjustment as the volume fraction is not very high, in such a way that the "soft" particulate system have a lower value of percolation threshold in terms of volume fraction over the "hard" one.

(8) Study on the conductivity over the various value of inclusion aspect ratio reveals the fact that the higher the aspect ratio is, the lower the effective conductivity, especially at high volume fraction. The discrepancies among conductivity for different cases are increasing during the compression process and reach the largest differences in the value of conductivity at the volume fraction of 80%.

(9) Analysis of the morphological shape of the ellipsoids (i.e. tri-axial ellipsoids, prolate, oblate) reveals that the prolate inclusions would produce the highest effective conductivity over the oblate particles or tri-axial ellipsoids at the highest volume fraction. The discrepancies in conductivity among them also increases with the volume fraction. The distinguished geometric characteristics of each particle are

account for this discrepancy in conductivity through the configurations of contact regions.

(10) The real material system is investigated by including interfacial friction and contact resistance among particles. It turns out the fact that both the contact area configuration and the contact resistance could affect the conductive properties significantly. The presence of interfacial friction would impede the relative motion among particles and result in local deformation on the particle surface. Also, it would lower the value of percolation threshold in terms of volume fraction due to the inhibitions in particle location adjustment at the relatively low volume fraction. The friction existence among particles could also reduce the oscillation in corresponded effective conductivity because the energy dissipation of the entire system would happen among the "coarse" interfaces over the "smooth" one. The conductivity of these cases is approaching the same value due to the tight constraint particles when the volume fraction is sufficiently high, although there are very small differences.

(11) Performing interfacial contact resistance study definitely give us an insight of the materials microstructure since the contact resistance is inevitable in the real material system. The gap conductance obviously decreased the effective conductivity. However, the conductivity is independent of gap conductance when it exceeds the value of 10^3.

The simulation results involving gap conductance in this study cannot be made comparisons with the research on the two-phase interfacial effect of other authors because the mechanic's information of the contact resistance in our current study is different with others' work. Our particulate system present a convenient way to represent

the microstructure of the materials. In the manufacturing process, the particles configurations, the orientation angles of the grains, and the local deformation could be altered through different procedure used in producing materials. These factors could definitely change the overall mechanical properties of materials. Thus, investigation of the mechanical behavior of materials is, in turn, strongly beneficial in manufacturing and design.

4.2 Future Work

In order to represent a more realistic material system, development of a complex model incorporating the second phase (inclusion-matrix) with interfacial contact issues is the main objective in this research. Also, the value of contact resistance was assumed to be constant once the surfaces come to contact. Thus the future work will involve modeling the pressure-dependent contact resistance.

The thermal expansion is set to be zero during the entire process in this study to avoid particle expansion in the presence of temperature gradient. However, in the real material system, thermal expansion is inevitable, and the stability of the electrophysical properties influenced by temperature variations is a primary property of the materials [55]. Also, the thermal expansion coefficient varies among constituents in composites. A study [52] investigated the relations between thermal effects and composites with carbon fiber as the fillers present the fact that there was an increment in the resistance of the composite as the presence of thermal expansion. They concluded that the contacts between conductive materials would be impeded through the presence thermal expansion coefficient of the matrix. Future works will include this part of effects in a more

advanced model attempting to perform analyses on mechanical and thermodynamic processes.

References

1. Maleki, Hossein, J. Robert Selman, R. B. Dinwiddie, and H. Wang. "High thermal conductivity negative electrode material for lithium-ion batteries."*Journal of power sources* 94, no. 1 (2001): 26-35.

2. Striebel, K. A., A. Sierra, J. Shim, C-W. Wang, and A. M. Sastry. "The effect of compression on natural graphite anode performance and matrix conductivity." *Journal of Power Sources* 134, no. 2 (2004): 241-251.

3. Gnanaraj, J. S., Yaron S. Cohen, M. D. Levi, and D. Aurbach. "The effect of pressure on the electroanalytical response of graphite anodes and LiCoO 2 cathodes for Li-ion batteries." *Journal of Electroanalytical Chemistry* 516, no. 1 (2001): 89-102.

4. Wang, C-W., Y-B. Yi, A. M. Sastry, J. Shim, and K. A. Striebel. "Particle compression and conductivity in Li-ion anodes with graphite additives."*Journal of the Electrochemical Society* 151, no. 9 (2004): A1489-A1498.

5. Maleki, Hossein, J. Robert Selman, R. B. Dinwiddie, and H. Wang. "High thermal conductivity negative electrode material for lithium-ion batteries."*Journal of power sources* 94, no. 1 (2001): 26-35

6. Torquato, Salvatore, Thomas M. Truskett, and Pablo G. Debenedetti. "Is random close packing of spheres well defined?." *Physical review letters* 84, no. 10 (2000): 2064.

7. Scott, G. D., and D. M. Kilgour. "The density of random close packing of spheres." *Journal of Physics D: Applied Physics* 2, no. 6 (1969): 863.

8. Pouliquen, O., M. Nicolas, and P. D. Weidman. "Crystallization of non-Brownian spheres under horizontal shaking." *Physical Review Letters* 79, no. 19 (1997): 3640.

9. Jodrey, W. S., and E. M. Tory. "Computer simulation of close random packing of equal spheres." *Physical review A* 32, no. 4 (1985): 2347.

10. Tobochnik, Jan, and Phillip M. Chapin. "Monte Carlo simulation of hard spheres near random closest packing using spherical boundary conditions."*The Journal of chemical physics* 88, no. 9 (1988): 5824-5830.

11. Visscher, William M., and M. Bolsterli. "Random packing of equal and unequal spheres in two and three dimensions." *Nature* 239 (1972): 504-507.

12. Jeffrey C. Lagarias. *The Kepler Conjecture: The Hales-Ferguson Proof* 2011

13. Kansal, Anuraag R., Salvatore Torquato, and Frank H. Stillinger. "Computer generation of dense polydisperse sphere packings." *The Journal of chemical physics* 117, no. 18 (2002): 8212-8218.

14. Lubachevsky, Boris D., and Frank H. Stillinger. "Geometric properties of random disk packings." *Journal of statistical Physics* 60, no. 5-6 (1990): 561-583.

15. Donev, Aleksandar, Ibrahim Cisse, David Sachs, Evan A. Variano, Frank H. Stillinger, Robert Connelly, Salvatore Torquato, and Paul M. Chaikin. "Improving the density of jammed disordered packings using ellipsoids."*Science* 303, no. 5660 (2004): 990-993.

16. Bezrukov, Alexander, Monika Bargiel, and Dietrich Stoyan. "Statistical analysis of simulated random packings of spheres." *Particle & Particle Systems Characterization* 19, no. 2 (2002): 111.

17. Williams, S. R., and A. P. Philipse. "Random packings of spheres and spherocylinders simulated by mechanical contraction." *Physical Review E*67, no. 5 (2003): 051301.

18. Cheng, X., and A. M. Sastry. "On transport in stochastic, heterogeneous fibrous domains." *Mechanics of materials* 31, no. 12 (1999): 765-786.

19. Mohanty, Sitakanta, and Mukul M. Sharma. "A Monte Carlo RSRG method for the percolation/conduction properties of correlated lattices." *Physics Letters A* 154, no. 9 (1991): 475-481.

20. Hashin, Zvi. "Analysis of composite materials—a survey." Journal of Applied Mechanics 50, no. 3 (1983): 481-505.

21. Torquato, Salvatore. "Random heterogeneous media: microstructure and improved bounds on effective properties." *Applied mechanics reviews* 44, no. 2 (1991): 37-76.

22. Chen, Jian, Limei Xu, and Hui Li. "Investigation on a direct modeling strategy for the effective elastic moduli prediction of composite material." *Materials Science and Engineering: A* 491, no. 1 (2008): 385-389.

23. Hashin, Zvi, and Shmuel Shtrikman. "A variational approach to the theory of the effective magnetic permeability of multiphase materials." *Journal of applied Physics* 33, no. 10 (1962): 3125-3131.

24. Yi, Y-B., and A. M. Sastry. "Analytical approximation of the percolation threshold for overlapping ellipsoids of revolution." In *Proceedings of the Royal Society of London A: Mathematical, Physical and Engineering Sciences*, vol. 460, no. 2048, pp. 2353-2380. The Royal Society, 2004.

25. Berhan, L., Y. B. Yi, A. M. Sastry, E. Munoz, M. Selvidge, and R. Baughman. "Mechanical properties of nanotube sheets: Alterations in joint morphology and achievable moduli in manufacturable materials." *Journal of Applied Physics* 95, no. 8 (2004): 4335-4345.

26. Zhang, T., and Y. B. Yi. "Monte Carlo simulations of effective electrical conductivity in short-fiber composites." *Journal of applied physics* 103, no. 1 (2008): 014910.

27. Yi, Y. B. "Void percolation and conduction of overlapping ellipsoids."*Physical Review E* 74, no. 3 (2006): 031112.

28. Yi, Y. B., L. Berhan, and A. M. Sastry. "Statistical geometry of random fibrous networks, revisited: waviness, dimensionality, and percolation."*Journal of applied physics* 96, no. 3 (2004): 1318-1327.

29. Berhan, L., Y. B. Yi, A. M. Sastry, E. Munoz, M. Selvidge, and R. Baughman. "Mechanical properties of nanotube sheets: Alterations in joint morphology and achievable moduli in manufacturable materials." *Journal of Applied Physics* 95, no. 8 (2004): 4335-4345.

30. Berhan, L., and A. M. Sastry. "Modeling percolation in high-aspect-ratio fiber systems. I. Soft-core versus hard-core models." *Physical Review E* 75, no. 4 (2007): 041120.

31. Torquato, Salvatore. *Random heterogeneous materials: microstructure and macroscopic properties*. Vol. 16. Springer Science & Business Media, 2013.

32. MAXWELL, A. "JC:'A treatise on electricity and magnetism Vol. II'." (1873).

33. Gubernatis, J. E., and J. A. Krumhansl. "Macroscopic engineering properties of polycrystalline materials: Elastic properties." *Journal of Applied Physics*46, no. 5 (1975): 1875-1883.

34. Wei, Chenyu, Deepak Srivastava, and Kyeongjae Cho. "Structural ordering in nanotube polymer composites." *Nano letters* 4, no. 10 (2004): 1949-1952.

35. McLaughlin, R. "A study of the differential scheme for composite materials." *International Journal of Engineering Science* 15, no. 4 (1977): 237-244.

36. Tawerghi, Elyas, and Yun-Bo Yi. "A computational study on the effective properties of heterogeneous random media containing particulate inclusions."*Journal of Physics D: Applied Physics* 42, no. 17 (2009): 175409.

37. Mondescu, Radu P., and M. Muthukumar. "Statistics of an ideal polymer in a multistable potential: exact solutions and instanton approximation." *The Journal of chemical physics* 110, no. 24 (1999): 12240-12249.

38. Garboczi, Edward J., and James G. Berryman. "Elastic moduli of a material containing composite inclusions: effective medium theory and finite element computations." *Mechanics of Materials* 33, no. 8 (2001): 455-470.

39. Cheng, X., A. M. Sastry, and B. E. Layton. "Transport in stochastic fibrous networks." *Journal of engineering materials and technology* 123, no. 1 (2001): 12-19.

40. Wang, Hongyu, Masaki Yoshio, Takeshi Abe, and Zempachi Ogumi. "Characterization of carbon-coated natural graphite as a lithium-ion battery anode material." *Journal of The Electrochemical Society* 149, no. 4 (2002): A499-A503.

41. Okada, Hiroshi, Yasuyoshi Fukui, and Noriyoshi Kumazawa. "Homogenization method for heterogeneous material based on boundary element method." *Computers & Structures* 79, no. 20 (2001): 1987-2007.

42. Pike, G. E., and C. H. Seager. "Percolation and conductivity: A computer study. I." *Physical review B* 10, no. 4 (1974): 1421.

43. Torquato, S., and M. D. Rintoul. "Effect of the interface on the properties of composite media." *Physical Review Letters* 75, no. 22 (1995): 4067.

44. Miloh, T., and Y. Benveniste. "On the effective conductivity of composites with ellipsoidal inhomogeneities and highly conducting interfaces." In *Proceedings of the Royal Society of London A: Mathematical, Physical and Engineering Sciences*, vol. 455, no. 1987, pp. 2687-2706. The Royal Society, 1999.

45. Wei, En-Bo, and Y. M. Poon. "Effective thermal conductivity of graded nonlinear composites with heat contact resistance." *Physics Letters A* 359, no. 6 (2006): 685-692.

46. Benveniste, Y. "A general interface model for a three-dimensional curved thin anisotropic interphase between two anisotropic media." *Journal of the Mechanics and Physics of Solids* 54, no. 4 (2006): 708-734.

47. Seaton, N. A., and Eduardo D. Glandt. "Monte Carlo simulation of adhesive disks." *The Journal of chemical physics* 84.8 (1986): 4595-4601.

48. Nayak, Rajlakshmi, Dora P. Tarkes, and Alok Satapathy. "A computational and experimental investigation on thermal conductivity of particle reinforced epoxy composites." *Computational Materials Science* 48, no. 3 (2010): 576-581.

49. Hasselman, D. P. H., and Lloyd F. Johnson. "Effective thermal conductivity of composites with interfacial thermal barrier resistance." *Journal of Composite Materials* 21, no. 6 (1987): 508-515.

50. Douglas, Jr, Jim, and Thomas F. Russell. "Numerical methods for convection-dominated diffusion problems based on combining the method of characteristics with finite element or finite difference procedures." *SIAM Journal on Numerical Analysis* 19, no. 5 (1982): 871-885.

51. Shimada, Kenji, and David C. Gossard. "Automatic triangular mesh generation of trimmed parametric surfaces for finite element analysis."*Computer Aided Geometric Design* 15, no. 3 (1998): 199-222.

52. Tzeng, Shinn-Shyong, and Fa-Yen Chang. "Electrical resistivity of electroless nickel coated carbon fibers." *Thin Solid Films* 388, no. 1 (2001): 143-149.

53. Yi, Y-B., C-W. Wang, and A. M. Sastry. "Compression of packed particulate systems: simulations and experiments in graphitic Li-ion anodes." *Journal of engineering materials and technology* 128, no. 1 (2006): 73-80.

54. Manual Comsol. "Comsol multiphysic user's guide." (2005).

55. Dobrovol'skaya, I. P., Z. Yu Chereiskii, K. E. Perepelkin, and B. M. Tarakanov. "Conductivity of Film Composite Materials Based on a Polymer Matrix and Carbon-Fibre Filler." *Fibre Chemistry* 35, no. 4 (2003): 302-305.